Tutorial on Describing, Classifying, and Visualizing Common Crystal Structures in Nanoscale Materials Systems

Katelyn J. Baumler and Raymond E. Schaak*

ACCESS | Metrics & More | Article Recommendations | SI Supporting Information

ABSTRACT: Crystal structures underpin many aspects of nanoscience and technology, from the arrangements of atoms in nanoscale materials to the ways in which nanoscale materials form and grow to the structures formed when nanoscale materials interact with each other and assemble. The impacts of crystal structures and their relationships to one another in nanoscale materials systems are vast. This Tutorial provides nanoscience researchers with highlights of many crystal structures that are commonly observed in nanoscale materials systems, as well as an overview of the tools and concepts that help to derive, describe, visualize, and rationalize key structural features. The scope of materials focuses on the elements and their compounds that are most frequently encountered as nanoscale materials, including both close-packed and nonclose-packed structures. Examples include three-dimensionally and two-dimensionally bonded compounds related to the rocksalt, nickel arsenide, fluorite, zincblende, wurtzite, cesium chloride, and perovskite structures, as well as layered perovskites, intergrowth compounds, MXenes, transition metal dichalcogenides, and other layered materials. Ordered versus disordered structures, high entropy materials, and instructive examples of more complex structures, including copper sulfides, are also discussed to demonstrate how structural visualization tools can be applied. The overall emphasis of this Tutorial is on the ways in which complex structures are derived from simpler building blocks, as well as the similarities and interrelationships among certain classes of structures that, at first glance, may be interpreted as being very different. Identifying and appreciating these structural relationships is useful to nanoscience researchers, as it allows them to deconstruct complex structures into simpler components, which is important for designing, understanding, and using nanoscale materials.

KEYWORDS: *crystal structures, solid state chemistry, layered structures, nanoscience, structural relationships, close-packed structures, perovskites, metal oxides, metal chalcogenides*
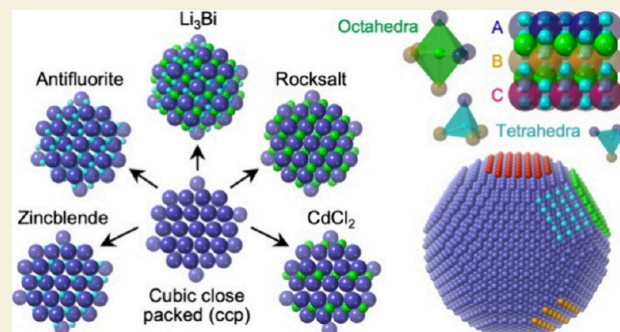
■ INTRODUCTION

The subdisciplines encompassed by nanoscience and nanotechnology are inherently diverse, spanning the physical and biological sciences as well as engineering and medicine. Nanoscale solids are foundational to these and many other research areas, including nanocrystals used for catalysis, medical diagnostics and therapeutics, energy conversion and storage, and flat panel displays, as well as in miniaturized devices and in applications that leverage their unique size- and shape-dependent physical properties. The way in which atoms arrange in solids—the "crystal structure"—defines how the atoms interact, which in turn defines the foundational properties of the solid.[1] For nanoscale solids, morphological features such as size, shape, and dimensionality can further modify these properties.[2] Additionally, at the surface of a nanoscale material, the arrangement of atoms is generally different when different crystal planes (facets) are exposed, as is the case for nanocrystals having different shapes. These structural differences can lead to differences in catalytic activity and selectivity, as well as to differences in surface chemistry and reactivity.[3−5] Crystal

structure also plays a prominent role in the synthesis of nanoscale materials. The arrangements of atoms in the smallest seeds that often form first can define the structure of the products, as well as the pathways by which they evolve and grow during synthesis.[6−8]

As a result of the breadth that is a hallmark of this interdisciplinary field, many nanoscience and nanotechnology researchers have not had the opportunity to study crystal structures in depth during their education and training, and therefore are not fully conversant with how crystal structures can be described systematically and how more complex crystal structures are derived from simpler structures. They may also be unaware of interrelationships among structures, as well as subtle
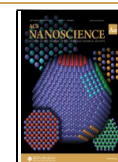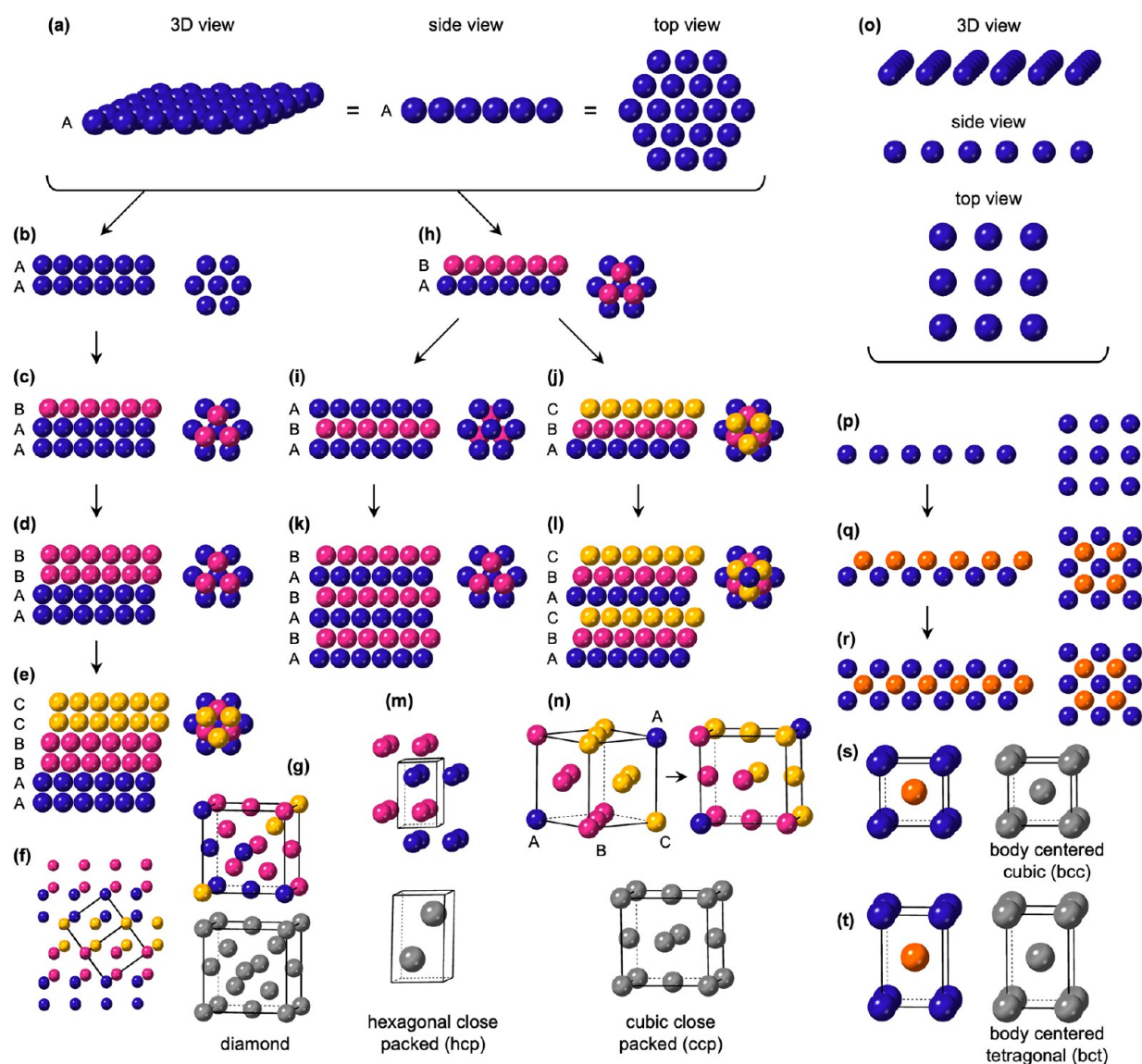
Figure 1. Derivation of common close-packed and nonclose-packed structures of the elements that are frequently encountered in nanoscale systems. (a) Structure of a close-packed layer, including equivalent three-dimensional (3D), side, and top views. (b) When two close-packed layers are stacked directly on top of one another (eclipsed), they form an AA bilayer. (c) When a third layer is staggered relative to the two below it, the stacking sequence is AAB. Adding another eclipsed layer on top of B forms (d) AABB, and adding another staggered layer followed by another eclipsed layer forms (e) AABBCC. Side and top views are shown in each panel. An expanded AABBCCAA side view is shown in (f), along with an overlaid unit cell. This unit cell, which is extracted and rotated in (g), corresponds to the diamond structure. The color coding corresponds to the close-packed layer from which the diamond structure is derived. Returning to the close-packed layers, if the second layer is staggered relative to the first, an AB stacking sequence results, as shown in (h). Two options for placing the third layer, relative to the first two, are possible. If the third layer is staggered relative to the second, but eclipses the first, an ABA stacking sequence results, as shown in (i). However, if the third layer staggers relative to both the first and second layers, an ABC stacking sequence results, as shown in (j). The ABABAB stacking sequence, expanded in (k), is referred to as hexagonal close packed (hcp), while the ABCABC stacking sequence, expanded in (l), is referred to as cubic close packed (ccp). The hcp unit cell is shown in (m) while the ccp unit cell is shown in (n). In (n), on the left-hand side, the color coding and orientation of the unit cell clarify the relationship to the ABCABC stacking sequence from which it is derived, while the right-hand side shows the same color coding but with the ccp unit cell (analogous to face centered cubic, fcc) in a more familiar orientation. Starting with a nonclose-packed cubic arrangement of atoms, shown in (o), we can similarly derive a body centered cubic (bcc) structure, as shown progressively in (p), (q), and (r). Here, the third layer always eclipses the first layer. The bcc unit cell is shown in (s), and a related body centered tetragonal unit cell, which is expanded in one direction relative to the other two, is shown in (t). In (g), (m), (n), (s), and (t), color-coded unit cells are shown simply to relate them to the stacked close-packed or nonclose-packed structures from which they are derived. Grayscale unit cells are also shown to better represent the actual structures, where each crystallographic site is equivalent.

(but important) differences among closely related structures. Given the central role of crystal structures in the synthesis, properties, and applications of various types of nanomaterials, it is important to understand these fundamental details for the structures that are most often encountered in nanoscale systems.

In this Tutorial, we aim to equip researchers from across the breadth of the nanoscience and nanotechnology communities with the language of crystal structures at a level that is approachable and insightful. For those who already have familiarity with crystal structures, we hope that these concise highlights will refresh and inspire. We begin with the simplest

crystal structures—those of the elements that are frequently encountered as nanoscale metallic and semiconducting materials—to introduce vocabulary, concepts, and visualization strategies, as well as examples of how crystal structures translate to frequently observed nanoscopic features. We then begin deriving common crystal structures from these simpler structures of the elements. To do so, we show how the structures of binary, ternary, quaternary, and more compositionally complex compounds systematically evolve through the presence or absence of different atoms filling holes in parent structures, as well as through other modifications at precise locations within the structures. These examples allow us to highlight interrelationships among common crystal structures and to provide a cohesive framework by which to analyze and understand them. Finally, we provide a more in-depth comparative overview of several families of crystal structures that are common among nanoscale materials systems. Throughout these examples, we highlight common misconceptions and fill in knowledge gaps involving crystal structures that are frequently encountered in the growing literature of nanoscale materials systems.

This Tutorial is intended as an overview of crystal structures and the ways in which they can be visualized and compared. It includes a lot of information but is purposely not exhaustive. Rather, it focuses on instructive examples that highlight key structural interrelationships. Our hope is that readers can apply similar structural analyses to the systems they are studying so that they can gain deeper understanding of them while also sparking new ideas and insights. Readers are directed to more comprehensive resources for a thorough treatment of the topics;[9−18] in many cases, these resources have inspired the content we chose to include and emphasize in this Tutorial. Readers are also directed to resources on complementary topics involving characterizing materials and their crystal structures.[19,20]

Throughout this Tutorial, crystal structure graphics were generated using the CrystalMaker software package.[21] Crystal-Maker files for selected structures, labeled based on the figures to which they correspond, are provided in the Supporting Information to give readers the opportunity to interact with them, including rotating them to visualize them in different orientations. The free demo version of CrystalMaker, available online at https://crystalmaker.com/crystalmaker/download/index.html, may be used to open and view the files. Accompanying CIF files (CIF = crystallographic information file) are also included in the Supporting Information for users who have access to other structure visualization software. Crystallographic data for all structures included in the Supporting Information was obtained from Pearson's Handbook of Crystallographic Data and the Materials Project.[22,23] Additionally, Figures S1 through S13 in the Supporting Information contain selected crystal structures from throughout this Tutorial with crystallographic axes superimposed so that the orientations in which they are shown can be correlated with their unit cells.

STRUCTURES OF THE ELEMENTS

Many crystal structures, including those of most of the elements,[16] are derived from planes of atoms that are arranged in a way that maximizes their packing efficiencies. Figure 1a shows a "close-packed" plane, along with a top-down view to highlight the arrangement of the atoms in this plane. We can stack two close-packed planes directly on top of one another

(Figure 1b), but doing so is inefficient, as it does not maximize the fraction of space that is filled. Rather, there is significant open space between atoms in this "eclipsed" geometry and the resulting density is low. If we label the vertical registry as "A", then two close-packed planes stacked directly on top of one another (i.e., eclipsed) will have a stacking configuration of "AA". ("Vertical registry" refers to the relative positions of subsequent stacked layers relative to the first layer.) Each close-packed plane has depressions in it created by the curvature of the spheres that represent the atoms. It is preferable to stagger one close-packed plane relative to the other rather than to stack them such that they are eclipsed. If a subsequent close-packed plane shifts relative to the one below it such that the bottom of the second layer of spheres rests in the depressions at the top of the first layer of spheres, we designate this shifted vertical registry as "B". If we place a staggered close-packed layer on top of our two eclipsed layers from Figure 1b, we now have an arrangement of "AAB", shown in Figure 1c. If we add another eclipsed close-packed layer, we now have "AABB" (Figure 1d). If we instead wish to add another staggered close-packed layer, there are two closely related, but distinct, options for where it can sit from the perspective of vertical registry. It can either sit directly on top of the "A" layer that is below, or it can shift slightly and sit such that it defines a new vertical registry (relative to the previous layers), i.e., "C". Figure 1e shows two "C" layers placed on top of "AABB" to generate "AABBCC".

For readers who are already familiar with close-packed structures, it may seem a bit odd to begin with a stacking sequence of "AABBCC". However, this stacking sequence allows us to define a common crystal structure, diamond. The diamond crystal structure, adopted by carbon as well as the ubiquitous semiconductors silicon and germanium, can be described as an "AABBCC" stacking sequence of close-packed planes. A unit cell, which is the smallest repeating unit of the crystal structure that can generate the entire crystal structure simply through translation (and not rotation), can be excised from the larger "AABBCC" structure to show the familiar diamond structure (Figure 1f). Rotating the diamond unit cell, with a few other atoms in adjacent unit cells shown for clarity, helps to visualize the "AABBCC" stacking sequence within diamond (Figure 1g).

Returning to the single close-packed plane in Figure 1a, we can place a second close-packed layer staggered relative to the first, creating the "AB" stacking sequence shown in Figure 1h that contrasts with the "AA" stacking sequence shown in Figure 1b. As was the case for the "AABB" example in Figure 1d, we have two options for where to place a third layer on top of the "AB" layers in Figure 1h. We can choose to stack the new close-packed plane directly above the "A" layer, forming "ABA" (Figure 1i) or in a new vertical registry to form "ABC" (Figure 1j). Continuing these sequences, we end up with either "ABABAB" (Figure 1k) or "ABCABC" (Figure 1l). The "ABABAB" stacking sequence is commonly known as "hexagonal close packed" or "hcp" and the "ABCABC" stacking sequence is "cubic close packed" or "ccp". Taking the hcp structure, which is adopted by metals such as Mg, Ti, Re, and Ru, the hexagonal unit cell in Figure 1m can be defined. This common depiction of the hcp unit cell makes it challenging to visualize the close-packed structure from which it is derived, but it is important to remember this relationship. Using a similar approach, in Figure 1n we define a unit cell for the ccp structure, which is adopted by most of the elemental metals that are encountered in nanoscale systems, including Ni, Cu, Rh, Pd, Ag, Ir, Pt, Au, Al, and Pb. This cubic unit cell is also known as "face
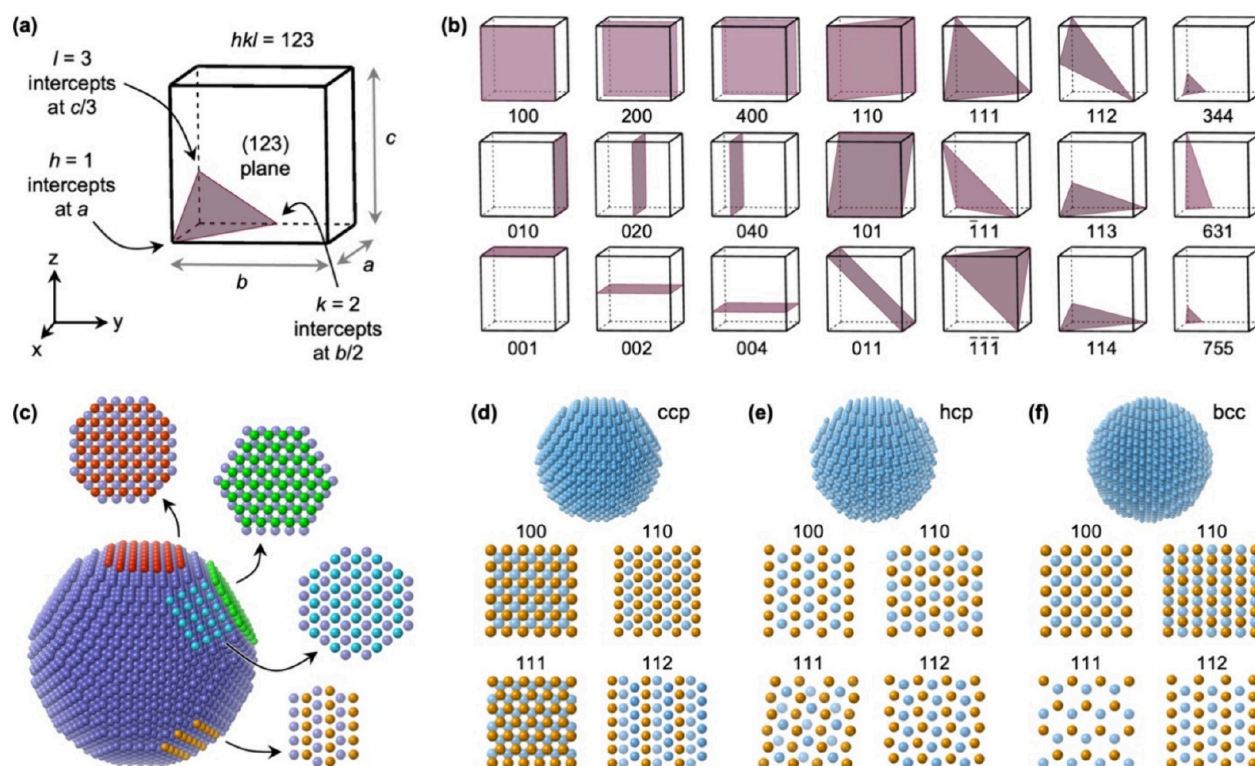
Figure 2. Descriptions and visualizations of crystal planes and facets. (a) A generic unit cell oriented relative to the *x*, *y*, and *z* axes and showing the unit cell dimensions *a*, *b*, and *c*. A crystallographic plane that intercepts the *x*, *y*, and *z* axes at *a*, *b*/2, and *c*/3 is shown; this plane corresponds to the Miller index (123). (b) A series of crystallographic planes are shown, including low-index and high-index planes, as well as series of related planes for comparison. (c) The structure of a hypothetical single-crystal fcc nanoparticle is shown, along with the surface structures (assuming no reconstruction) of four different facets. The surface atoms are color coded; the atoms in the layer directly below the surface layer are included as well, colored light purple. Structures of hypothetical single-crystal fcc, hcp, and bcc nanoparticles are shown in (d), (e), and (f), respectively, along with the structures of the (100), (110), (111), and (112) planes. For each plane, the atoms in one layer are shown in orange while atoms in a layer directly below are shown in light blue.

centered cubic" (fcc). Here we recognize that ccp and fcc are often used synonymously, although as will be discussed below, they are truly equivalent only when there is only one element, i.e., for elemental metal systems. The fcc unit cell contains four layers of the ccp structure, stacked "ABCA" along the body diagonal (i.e., the diagonal line running from one corner of the unit cell to the opposite corner); the color coding in Figure 1n helps to highlight this relationship.

Considering the elements that are most frequently studied as nanoscale materials, it is important to introduce two other crystal structures that are not derived from the stacking of close-packed planes. (Some elements adopt additional distinct crystal structures that will not be discussed here.) If we begin with a cubic (instead of close-packed) arrangement of atoms in a single layer (Figure 1o,p) and stagger subsequent layers relative to the one below it (Figure 1q,r), we define the "body centered cubic" (bcc) structure, which is adopted by elements that include Li, V, Cr, Fe, Nb, Mo, and W. The bcc unit cell is shown in Figure 1s. Stretching the bcc unit cell vertically produces a "body centered tetragonal" (bct) variant (Figure 1t), which is adopted by In and one form of Sn.

The unit cells shown in Figure 1 represent cubic, tetragonal, and hexagonal systems. There are seven lattice systems—cubic, tetragonal, orthorhombic, hexagonal, rhombohedal, monoclinic, and triclinic—from which 14 Bravais lattices are defined. For example, within the cubic system, there can be primitive cubic, body-centered cubic, and face-centered cubic Bravais lattices. It is important to note that lattice systems and Bravais lattices are

not crystal structures; they define the three-dimensional periodic arrays of lattice points onto which a "basis" (the arrangement of atoms on each lattice point) is placed. It is therefore insufficient to refer to a crystal structure as "cubic" or "tetragonal" or "hexagonal" without further qualification or context. For example, elemental metals that are fcc are said (by convention) to adopt the Cu structure type, because Cu is the name given to a crystal structure generated by placing a single type of atom (basis) on each of the fcc lattice points. Elemental silicon also has a fcc lattice, but its basis is different, and therefore its crystal structure ("diamond", named after the carbon variant) is different.

CRYSTALLOGRAPHIC PLANES, DIRECTIONS, AND FACETS

Now that we have discussed the crystal structures of many of the elements, it is useful to consider how these crystal structures translate to nanoscale features. One of the hallmarks of nanocrystal chemistry is the ability to access different shapes, which can have different properties such as surface plasmon resonance frequencies[24] or catalytic activities and/or selectivities.[25,26] Synthetic control of nanocrystal shape is often achieved by using different surfactants and/or reaction conditions that slow down or accelerate growth in certain crystallographic directions, based on a complex interplay between surface energies and ligand binding strengths.[2] It is therefore important to have a framework for labeling and discussing the different crystal planes, facets, and directions.[27]
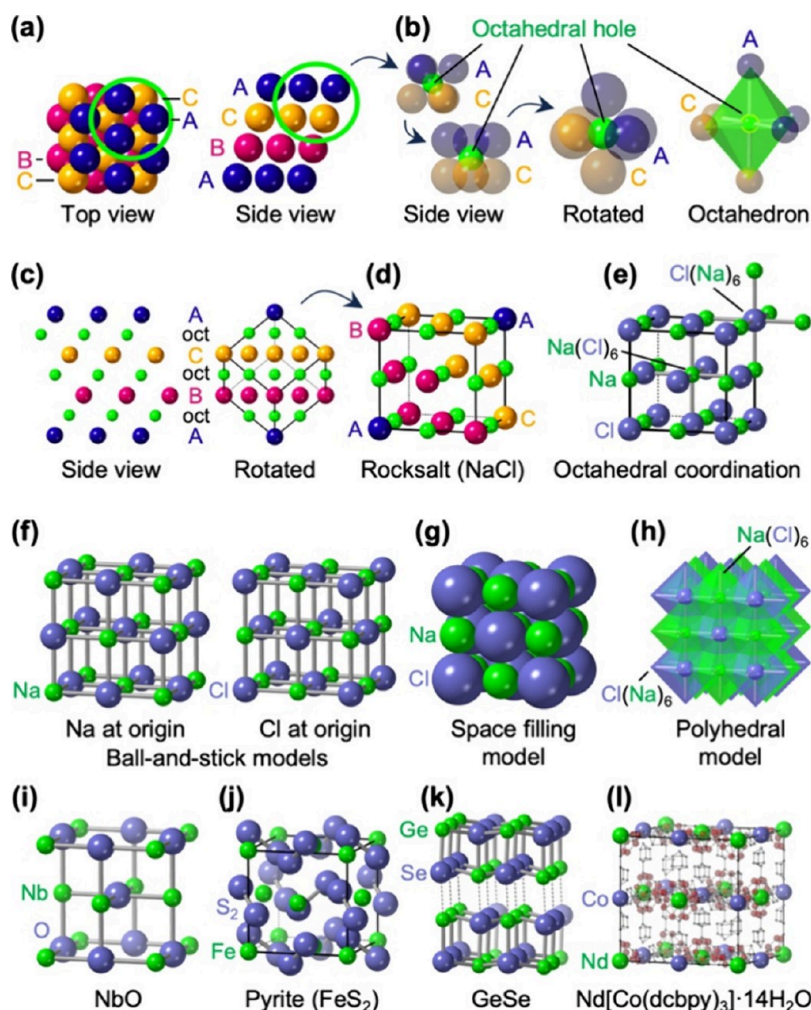
Figure 3. Derivation of NaCl (rocksalt) and NaCl-related structures. (a) Top view and side view of an ABC stacking sequence of close-packed layers, indicating the relative positions of the A (dark blue), B (pink), and C (yellow-orange) layers. The green circles highlight the location (in both the top view and the side view) of a single octahedral hole. The location and coordination environment are further highlighted in (b), which shows the same crystallographic site in various orientations and moving from a filled octahedral hole between close-packed layers to a familiar octahedron with an atom in the center. Different side views are shown in (c). Here, the locations of all octahedral holes in an ABC (ccp) stacking sequence of close-packed layers are shown. In the rotated structure in (c), the unit cell of NaCl (rocksalt) is shown. The unit cell is rotated to adopt a more familiar orientation in (d), while retaining the color coding that correlates to the A, B, and C close-packed layers from which it is derived. In (e), the same unit cell orientation is shown, now color coded according to the identities of the atoms (Na = green, Cl = purple). The octahedral coordination environments for both the Na and Cl are highlighted. Two versions of the NaCl unit cell are shown in (f); both unit cells are drawn in a ball-and-stick model which emphasizes both the atoms and the interactions between atoms. One unit cell has chlorine at the origin while the other has sodium at the origin. A space filling model in the same orientation is shown in (g), along with a polyhedral model in (h) that includes all constituent octahedra. Several NaCl-derived and NaCl-related structures are also shown: (i) NbO, (j) pyrite FeS_2, (k) GeSe, and (l) the metal−organic hybrid compound $Nd[Co(dcbpy)_3]\cdot14H_2O$.

Figure 2 shows some of the planes that are frequently encountered for various types of crystal structures, as they are often exposed on the outer surfaces of nanocrystals having different shapes and faceting. The labels for each plane represent their "Miller index", or (hkl) value, which uniquely defines them. Here, it is useful to recognize that h, k, and l are integers and that they correlate with a, b, and c, respectively, which are the lattice constants of the unit cell that are in the directions of the x, y, and z axes, respectively (Figure 2a). The Miller index "h" means that the plane to which it corresponds extends $1/h$ of the way along the x-axis to the edge of the unit cell, and therefore has a distance between planes of a/h. Likewise, "k" extends $1/k$ of the way along the y-axis to the edge of the unit cell and has a distance between planes in that direction of b/k, and "l" extends $1/l$ of the way along the z-axis to the edge of the unit cell and has a distance between planes in that direction of c/l. Accordingly, the (222)

plane is defined by the following three points in the unit cell: $1/2$ along a, $1/2$ along b, and $1/2$ along c. A h, k, or l value of "1" means that the plane crosses the unit cell at a distance of a, b, or c, respectively, relative to the origin. As an example, the (123) plane, which intersects the unit cell at a, $b/2$, and $c/3$, is shown in Figure 2a. A h, k, or l value of "0" means that the plane includes that axis. For example, the (001) plane is the a-b plane that includes the x and y axes, and the distance between the (001) planes is equal to c, or the lattice constant in the z-axis direction. Likewise, the (111) plane is the body diagonal and the (101) plane includes the y-axis and is the face diagonal.

Figure 2b shows several planes for a cubic unit cell with their corresponding Miller indexes. The examples shown include both "low index" planes (where h, k, and l are small integers, typically 0 and 1) and "high index" planes (where h, k, and l are larger integers); the latter are often sought after in catalysis because of

their lower coordination numbers and different interatomic distances.[28] Figure 2b also shows examples of parallel and nonparallel planes. The (100), (200), and (400) planes are parallel to one another, but have different interplanar spacings of a, $a/2$, and $a/4$, respectively. When some index numbers change but others do not, the planes are not parallel, as demonstrated with the (111), (112), (113), and (114) planes in Figure 2b. There can also be negative integers that comprise (hkl) (denoted by an overline), which orients the planes in different directions. For example, (111), ($\bar{1}$11), and ($\bar{1}\bar{1}\bar{1}$) all have the same interplanar spacings and are all part of the {111} family of planes (with brackets denoting families of equivalently spaced planes), but with different orientations depending on where they intersect the axes.

To demonstrate the importance of different crystallographic planes translating to different facets that could have distinct catalytic activities and selectivities, we show in Figure 2c an example of a multifaceted nanocrystal of a fcc metal. Here, the faceting exposes planes with different (hkl) values, and the corresponding structures of the surfaces of the ideal exposed planes (assuming no reconstruction) are shown. As can be seen, the structures of the surfaces are quite different, with a range of atom arrangements and interatomic spacings. It is worth noting that a crystallographic direction is distinct from a crystal plane. Crystallographic directions, which are denoted by square brackets, are perpendicular to the planes having the same (hkl) values.

When analyzing nanocrystalline materials to determine the planes, facets, and directions, it is important to remember that the structure visualized by high-resolution transmission electron microscopy, which can show lattice fringes or be atomically resolved, may have a different orientation than the unit cell. Figures 2d, 2e, and 2f show depictions of metal nanocrystals having ccp, hcp, and bcc structures, respectively. All three nanocrystals are oriented in the same direction based on the close-packed (for ccp and hcp) or cubic (for bcc) planes that stack vertically to create the 3D structure. The arrangements of atoms in various crystallographic planes are shown as well, along with the (hkl) values of these planes based on the unit cells. As can be seen, the atomic arrangements in planes corresponding to the same (hkl) values can be structurally very different for ccp vs hcp vs bcc, which is simply a consequence of the different orientations and sizes of the unit cells for each structure. Figure 2d-f therefore demonstrates why it is important to consider and compare structurally similar regions in different crystals rather than simply rely on planes with the same (hkl) values, as these can be different for different structures and not always represent comparable regions.

CLOSE-PACKED STRUCTURES WITH FILLED OCTAHEDRAL HOLES

We have discussed how the crystal structures of many of the elements can be derived by stacking close-packed planes in different sequences. Now we can turn to multielement compounds that can be described as derivatives of close-packed structures. In these crystal structures, additional atoms reside in the empty space ("holes") between the close-packed atoms. The systematic filling of these holes, in different ways and amounts, results in different crystal structures,[9,12,14] many of which are frequently adopted by nanoscale materials.

We begin by identifying and filling the octahedral holes in a ccp arrangement of close-packed atoms. Figure 3a shows both top and side views of the "ABCABC" ccp stacking sequence.

Enlarged regions, shown in Figure 3b, highlight the location and orientation of the octahedral hole relative to the atoms that comprise the close-packed planes. If we consider the atoms that comprise the close-packed structure to have an arbitrary radius of 1, then the hole in the center of the six-atom close-packed "pocket" can be ideally filled with an atom having a radius around 0.414. This smaller atom fills an octahedral hole, as the six larger close-packed atoms around it comprise an octahedron and the smaller atom sits at the center (Figure 3b). In most cases, anions are larger than cations, so anions generally constitute the larger atoms that comprise the close-packed structure while the smaller cations fill the holes. For every "packing atom", i.e., every atom that comprises the close-packed layers, there is one octahedral hole, such that the ratio of close packed atoms to octahedral holes is 1:1. It follows, then, that if every available octahedral hole is filled by cations in a close-packed structure of anions, then the cation:anion ratio will be 1:1. Figure 3c shows expanded views (in two orientations) of such a structure having all possible octahedral holes files, with each close-packed layer ("ABCA") represented as a different color. A unit cell extracted from this expanded structure, shown in Figure 3d, is one of the most common ionic crystal structures, rocksalt (NaCl). Indeed, if the anions are Cl$^-$ and the cations are Na$^+$, then the ccp array of Cl$^-$ anions with all octahedral holes filled by Na$^+$ cations defines the rocksalt structure; the color coding shows how the "ABCA" stacking sequence translates to the unit cell. Filling all of the octahedral holes with Na$^+$ cations in a ccp lattice of Cl$^-$ anions results in an array of corner-sharing octahedra with either Na$^+$ or Cl$^-$ at the center (Figure 3e). One interesting aspect of the rocksalt structure is that it can be described as two interpenetrating fcc lattices: one having Cl$^-$ at the origin and the other having Na$^+$ at the origin (Figure 3f).

The rocksalt structure, which is adopted by nanoscale materials such as PbS, PbSe, MnS, NiO, and TiN,[29−32] provides an instructive example for showcasing the different representations of crystal structures that are commonly depicted in nanoscale materials systems. For example, Figure 3f shows ball-and-stick models that emphasize the connections between atoms while Figure 3g shows a space filling model that better highlights the relative sizes and interconnectedness of the constituent ions. Figure 3h presents a polyhedral view that emphasizes both types of octahedra (Cl-centered and Na-centered) and their connections to one another. All views of the structure are useful, and being able to switch back and forth among them can be helpful as one seeks to visualize, emphasize, and/or understand various features and interrelationships within the crystal.

The rocksalt structure also provides an opportunity to highlight more complex crystal structures that can be described as derivatives. Figures 3i-l show several examples. NbO can be generated from rocksalt by removing the cations on the top and bottom faces and the anions on the side edges, relative to the Na-origin structure in panel (f) (Figure 3i). Pyrite (FeS$_2$) can be derived from rocksalt by replacing each anion with an anionic dimer (S$_2{}^{2-}$) centered where the anion in rocksalt was located (Figure 3j). SnS, SnSe, GeS, and GeSe[33] adopt a distorted rocksalt structure with a series of longer and shorter bonds (Figure 3k). The distorted structure arises from the presence of the $4s^2$ and $5s^2$ electrons in Ge^{2+} and Sn^{2+}, respectively, which are not significantly involved in bonding and therefore function as lone pairs.[33] The longer bonds are shown as dashed lines in Figure 3k, highlighting the pseudolayered structure that results. It is important to recognize, though, that the arrangement of
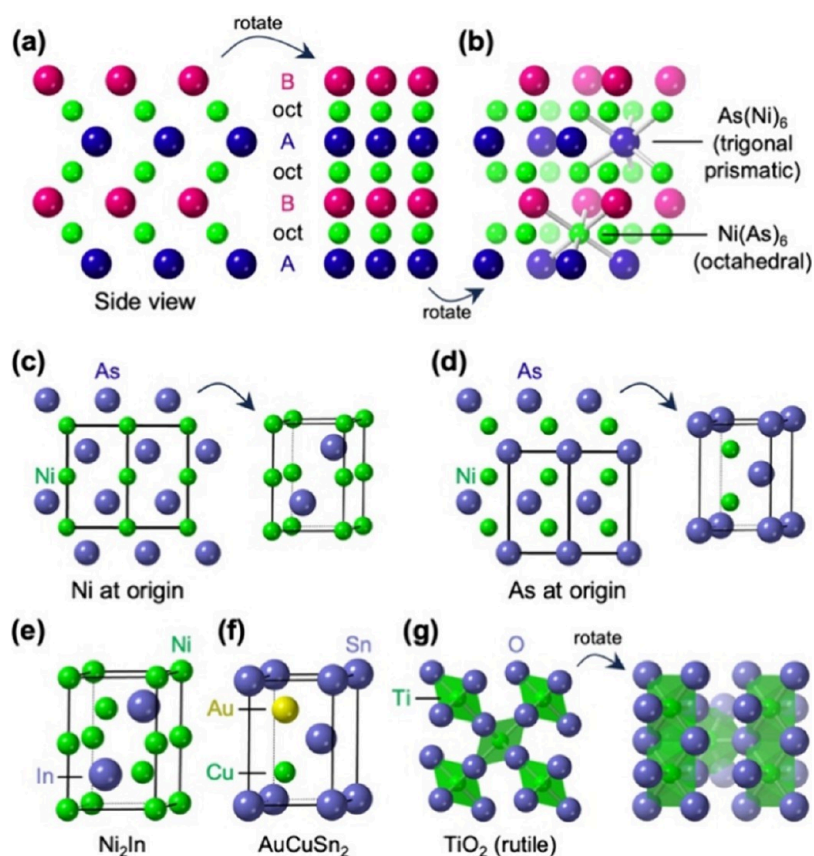
Figure 4. Derivation of NiAs and NiAs-related structures. (a,b) Depiction of an ABAB (hcp) stacking sequence of close-packed layers with all octahedral holes filled, which corresponds to the NiAs structure. Three side views with different rotation angles are shown; each highlights different characteristics of the structure. In (b), the presence of both octahedral and trigonal prismatic coordination environments is shown. The NiAs structure has two common unit cells: one, shown in (c), places Ni at the origin while the other, shown in (d), places As at the origin. Several variants of the NiAs structure are also shown: (e) Ni_2In, which has additional metal cations; (f) $AuCuSn_2$, which has ordered Au and Cu; and (g) rutile TiO_2, which fills only half of the octahedral holes in a distorted hcp anion structure.

atoms is still commensurate with a distorted rocksalt structure, which is composed of distorted octahedra, of which the apparent interlayer region is a part. Larger structures also adopt the rocksalt structure, including hybrid metal−organic crystals such as $Nd[Co(dcbpy)_3]\cdot14H_2O$ (dcbpy = 4,4′-dicarboxy-2,2′-bipyridine), where neodymium and cobalt occupy the cation and anion sites in rocksalt, with organic spacers that balance charge (Figure 3l).[34]

Recall that the rocksalt structure was derived by placing cations in all of the octahedral holes of a *ccp* lattice of anions. If we instead place cations in all of the octahedral holes of a *hcp* lattice of anions, we get the nickel arsenide (NiAs) crystal structure (Figure 4a). The only difference in how the NaCl (Figure 3c) and NiAs (Figure 4a) crystal structures are derived is the stacking sequence of the close-packed layers, i.e., ccp and hcp, respectively. However, this subtle structural difference translates to significant chemical differences that directly impact the types of compositions that prefer to adopt the NaCl versus NiAs structure types, as well as their properties and even how we tend to visualize the crystal structures at the unit cell level. As one example, the rocksalt structure has octahedral coordination for all cations and anions, while in the NiAs structure the cations have different coordination geometries than the anions. In NiAs, the cations still sit in the center of an octahedron formed by anions, but the anions sit in the center of a trigonal prism of cations (Figure 4b).

Two distinct unit cell depictions are common for the NiAs crystal structure and both are equivalent, differing only in whether cations (Figure 4c) or anions (Figure 4d) comprise the origin. Both unit cells are hexagonal and emphasize the key structural and chemical consequence of filling all octahedral holes in a hcp ("ABAB") lattice: the cations are eclipsed. Depending on the size of the anions in the close packed layers, the cations can be close enough to facilitate metal−metal bonding that directly impacts their electronic properties. Because of the proximity of the eclipsed cations, the NiAs structure disfavors highly ionic compounds, but rather is adopted by polar compounds that are less ionic. As an example, oxides having small cations with high charge densities will prefer the rocksalt structure while chalcogenides having transition metals capable of forming metal−metal bonding interactions will often be found to adopt the NiAs structure.

Many structural variants of NiAs exist, and many of these are observed in nanoscale systems. Figure 4e−g shows some examples; all are derived from NiAs by inserting or removing atoms at various places. For example, the Ni_2In structure inserts additional cations in interstitial sites within the close-packed planes of anions (Figure 4e). Various ordered motifs are also known, including $AuCuSn_2$ ($Au_{0.5}Cu_{0.5}Sn$) with alternating Au and Cu atoms on the metal sites (Figure 4f).[35] The rutile structure (Figure 4g), adopted by the ubiquitous photocatalyst TiO_2[36] as well as by IrO_2 and RuO_2, which are commonly used catalysts for the oxygen evolution reaction,[37] is a distorted
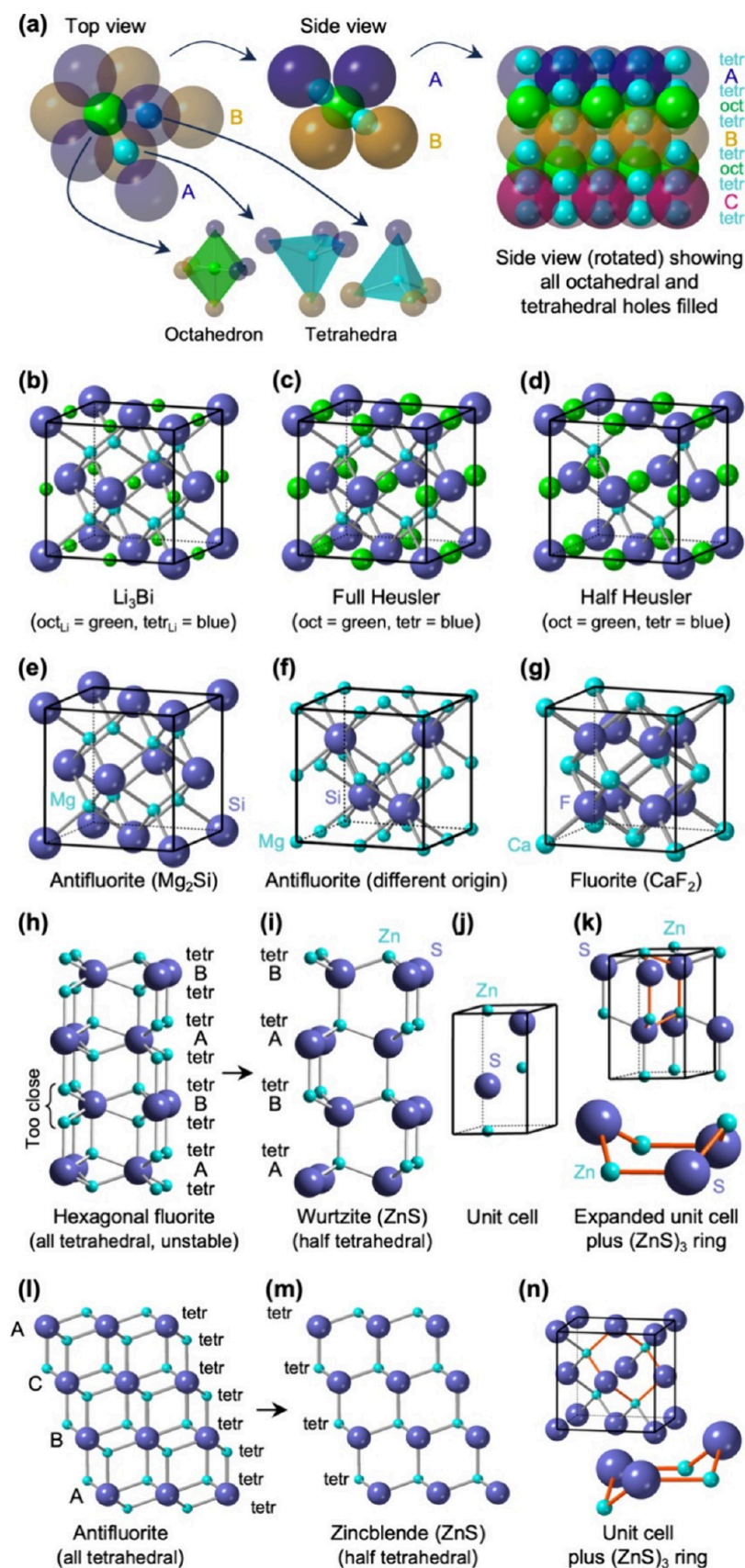
Figure 5. Crystal structures derived from full or partial occupancy of tetrahedral holes. (a) Top and side views of two close-packed layers, A (dark blue) and B (yellow-orange), showing one octahedral hole filled (with a large green sphere) and two distinct tetrahedral holes filled (with smaller light blue spheres). The corresponding polyhedra are shown, along with their locations within the close-packed layers. A side view with an ABC stacking sequence, showing all octahedral and tetrahedral holes filled, is also presented. Unit cells are shown for several structurally related phases, based on similarities and differences in how various tetrahedral and octahedral holes are filled: (b) Li_3Bi, (c) full Heusler, (d) half Heusler, (e,f) antifluorite

Figure 5. continued

Mg_2Si with two unit cells showing Si and Mg at the corners, respectively, and (g) fluorite CaF_2. The hypothetical hexagonal fluorite structure, based on an ABAB (hcp) stacking sequence, is shown in (h); this structure is generally unstable because of the close contact of the cations in the tetrahedral holes. The wurtzite structure is shown in (i). Wurtzite can be derived by removing half of the cations in alternating layers from the hexagonal fluorite structure in (h) and/or by filling half of tetrahedral holes, i.e., every other row, in an hcp arrangement of anions. The wurtzite unit cell is shown in (j), along with an expanded version in (k) that highlights the 6-membered Zn–S ring that comprises the structure. A different view of the antifluorite structure, which highlights the ABCABC stacking sequence of the close-packed layers, is shown in (l), along with the zincblende structure in (m). Zincblende can be derived by removing half of the cations in alternating layers from the fluorite structure in (l) and/or by filling half of the tetrahedral holes, i.e., every other row, in a ccp arrangement of anions. The zincblende unit cell is shown in (n), along with the 6-membered Zn–S ring that comprises the structure. The derivation of wurtzite and zincblende differ only in the stacking sequence of the close-packed layers: hcp for wurtzite and ccp for zincblende.

variant of NiAs. Rutile can be derived from NiAs by distorting the hcp anion lattice and filling only half of the octahedral holes, alternating in a checkerboard motif that results in edge sharing octahedra that are aligned in chains, with every other layer tilted in the opposite direction.

CLOSE-PACKED STRUCTURES WITH FILLED TETRAHEDRAL HOLES

We now switch to filling tetrahedral holes with cations in ccp and hcp anion lattices. While every packing atom in a close-packed structure was associated with one *octahedral* hole, as shown in Figure 3, there are two *tetrahedral* holes associated with each packing atom in a close-packed structure. The ideal radius for an atom occupying a tetrahedral hole, relative to a radius of 1 for each packing atom, is 0.225, which is smaller than the ideal radius of 0.414 for an atom filling an octahedral hole. Figure 5a shows top-down views of overlaid close-packed layers ("AB"), along with the locations of the octahedral and tetrahedral holes that exist between these layers. Figure 5a also shows side views of these same octahedral and tetrahedral holes, along with corresponding polyhedral views of the tetrahedra and octahedra. Since there are two tetrahedral holes per packing atom, there will be a 1:2 ratio of anions to cations if all tetrahedral holes are filled, assuming that the anions are larger and comprise the close packed layers. If all possible octahedral and tetrahedral holes are filled in a ccp structure, there will be one octahedral and two tetrahedral atoms per packing atom. The resulting formula is X_2YZ, where X and Y are the tetrahedral and octahedral cations, respectively, in a ccp lattice of Z anions. When the X and Y atoms are the same, the corresponding crystal structure is Li_3Bi (Figure 5b). When X and Y are different, the resulting structure is commonly known as a full Heusler compound, such as Cu_2MnAl (Figure 5c).[38] When all of the octahedral holes are filled but only half of the tetrahedral holes are filled alternately, the result is a half Heusler compound with a formula of XYZ, such as TiCoSb (Figure 5d).[38]

If all possible tetrahedral holes are filled with cations in a ccp lattice of anions and no octahedral holes are filled, we obtain the antifluorite structure, shown in Figure 5e. The antifluorite structure can be derived from the full Heusler structure by removing all of the atoms in the octahedral sites. Antifluorite is the structure adopted by many oxide and sulfide compounds having small alkali metal cations, such as Li_2O, Na_2S, and Mg_2Si. The antifluorite unit cell can be constructed with either the anion (Figure 5e) or the cation (Figure 5f) at the origin; each view emphasizes different characteristics of the structure. The fluorite structure (Figure 5g), which is named for the mineral CaF_2, has the positions of the anions and cations reversed relative to antifluorite. Fluorite therefore has a close-packed arrangement of cations with anions in all of the tetrahedral sites,

since the fluoride anion is quite small compared to cations such as Ca^{2+}. Compounds adopting the fluorite structure are common among nanostructured catalytic materials, including ceria (CeO_2) and zirconia (ZrO_2).[39,40] $NaYF_4$, a ubiquitous nanoparticle host material for rare earth dopants that leads to excellent upconversion properties,[41] also adopts the fluorite structure, with Na^+ and Y^{3+} randomly occupying the cation site, i.e., $Na_{0.5}Y_{0.5}F_2$.

Interestingly, the hcp analogue of fluorite and antifluorite—hcp close-packed layers with all of the tetrahedral holes filled—does not generally form. This instability can be rationalized by the electrostatic repulsion introduced by having eclipsed cations in close contact, as depicted in Figure 5h. If one removes half of the cations occupying the tetrahedral holes—specifically every other layer of tetrahedral cations so that there are no longer any that are directly eclipsed—this electrostatic repulsion and structural instability is removed. When one makes that modification, the commonly observed wurtzite crystal structure emerges (Figure 5i). The unit cell for wurtzite, shown in Figure 5j, emphasizes the hexagonal nature of the structure but de-emphasizes the longer-range structural features. Figure 5k also shows the wurtzite unit cell, but with a few additional atoms outside the boundary of the unit cell included. This view emphasizes the tetrahedral bonding and how the motif within the unit cell becomes the building block of the structure. Figure 5k also highlights a series of bonds within the wurtzite structure that form a six-membered ring; this ring is shown, enlarged and rotated, below the expanded unit cell. The six-membered ring extracted from the wurtzite structure contains three sets of alternating anions and cations, $(ZnS)_3$, in a motif that chemists will recognize as a "boat conformation"; this "boat conforma-tion" is one of the structures that can be adopted by the cyclohexane molecule.

Figures 5l-n show the same situation as for the *hcp* structure in Figures 5h-k, but now for a *ccp* structure. Figure 5l shows ccp close-packed layers with all of the tetrahedral holes filled; this arrangement corresponds to the antifluorite structure intro-duced in Figure 5e. If we remove alternating layers of atoms in tetrahedral holes, we are left with ccp anions having alternating layers of tetrahedral holes filled with cations, which corresponds to the commonly observed zincblende crystal structure (Figure 5m). Figure 5n shows the zincblende unit cell, which emphasizes the tetrahedral bonding. As we did for wurtzite in Figure 5k, we can define a six-membered ring of alternating anions and cations in the zincblende structure, as shown in Figure 5n. This $(ZnS)_3$ ring adopts a motif that chemists will recognize as a "chair conformation", which is another common structure observed for the cyclohexane molecule.

Zincblende and wurtzite differ only in the stacking sequence of the close-packed layers: "ABCABC" (ccp) for zincblende and
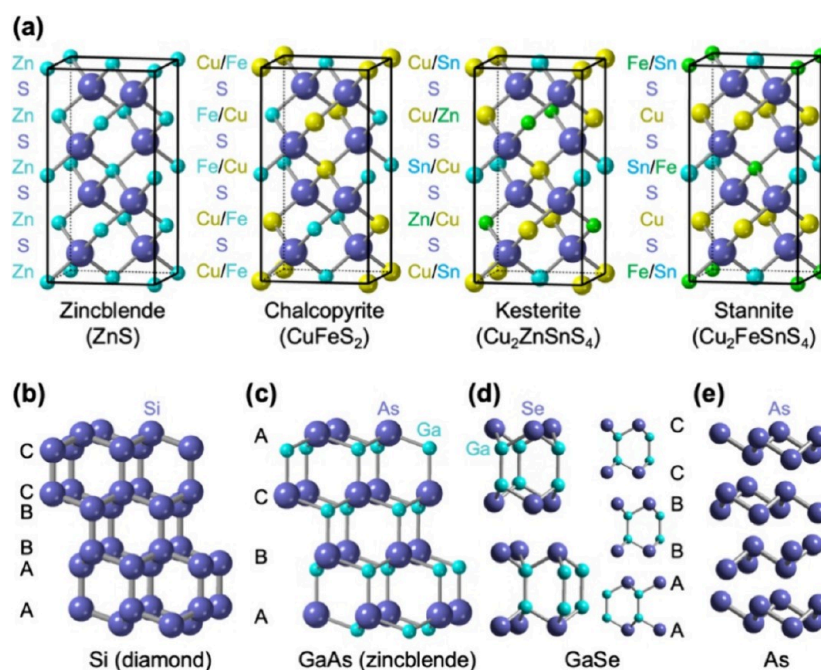
Figure 6. Crystal structures of diamond-like semiconductors. The crystal structure of zincblende ZnS (with a doubled unit cell) is shown in (a), along with several cation-ordered variants: chalcopyrite CuFeS$_2$, kesterite Cu$_2$ZnSnS$_4$, and stannite Cu$_2$FeSnS$_4$. The crystal structure of diamond is shown in (b), along with the related structures of (c) GaAs, (d) GaSe, and (e) As.

"ABAB" (hcp) for wurtzite. However, as was the case for the rocksalt versus NiAs structure types that similarly differed only in the stacking sequences of the close packed layers, the structural and chemical consequences of these stacking differences are significant. As one example of this significance, Figures 5k and 5n show the unit cells for zincblende and wurtzite, along with the connectivities of the anions and cations within the structure. Both are observed to form six-membered rings, as was discussed in the preceding paragraph. The "boat conformation" in wurtzite has eclipsed anions and cations in third nearest neighbor positions, which slightly favors more ionic compounds (due to electrostatic attraction), such as ZnO. In contrast, these same third nearest neighbors are not eclipsed in zincblende, favoring less ionic compounds such as the transition metal chalcogenides and halides. However, the energy differences between zincblende and wurtzite are small, and it is sometimes possible to selectively access both structures for a given composition, provided that one can find an appropriate synthetic pathway. Zincblende and wurtzite are the most commonly observed structures for the ubiquitous colloidal quantum dot materials CdS, CdSe, ZnS, and ZnSe, as well as GaN, GaP, InN, InP, GaAs, BN, InSb, and many others.[42−45] It is not surprising that these common II−V and III−V semiconductors adopt the zincblende and wurtzite crystal structures, as they are isoelectronic with Si and Ge. Si and Ge adopt the diamond structure, which also has exclusively tetrahedral coordination and can be described as zincblende where all atoms are identical (Figure 1f). Alternatively, zincblende can be described as the "AABBCC" diamond structure shown in Figure 1e, with alternating layers of anions (A, B, C) and cations (a, b, c), i.e., AaBbCc.

As for rocksalt and nickel arsenide that were shown in Figures 3 and 4, many variants of the zincblende and wurtzite structures exist, and they are common among nanoscale materials because of their semiconducting properties that lend well to applications in solar energy, photocatalysis, nanophotonics, nanoelectronics,

and sensing.[44−47] For example, chalcopyrite, kesterite, and stannite are cation-ordered variants of zincblende,[48] as shown in Figure 6a. Several are isoelectronic to silicon and germanium, which adopt the diamond structure (Figure 6b), as mentioned earlier. Interestingly, as one moves around the periodic table close to silicon and germanium, compounds that are isoelectronic generally adopt diamond-like (zincblende and/or wurtzite) crystal structures, as is the case for GaAs (Figure 6c). Upon replacing As in GaAs with Se, the resulting compound GaSe adopts a wurtzite-like structure that is layered (Figure 6d). The structure of GaSe can be described as an AABBCC arrangement of Se (mirroring the AABBCC arrangement in diamond-structured Si) with half of the tetrahedral holes filled—all of the tetrahedral holes within one AA, BB, or CC layer and none of the tetrahedral holes within the AB and BC layers. This reduction from three-dimensional bonding in GaAs to two-dimensional bonding in GaSe results from electronic effects and occurs by selectively removing both anions and cations in every other layer to maintain charge balance. Upon replacing Ga in GaAs with As to form AsAs (or As$_2$, or simply As), the electron count further increases and the structure further reduces in dimensionality (Figure 6e). Interestingly, the As chains retain their structural relationship to the GaAs parent compound. This progression through p-block tetrahedral semiconductors from Si to GaAs to GaSe to As nicely captures structural relationships among seemingly unrelated materials.

CRYSTAL STRUCTURES OF TWO-DIMENSIONALLY BONDED COMPOUNDS

The concept of systematically removing atoms in alternating layers, as described above, is common in crystal chemistry and leads to the emergence of some of the most prominent 2D materials studied in the nanoscience and nanotechnology communities. For example, if we start with either rocksalt (ccp) or NiAs (hcp) and remove every other layer of cations filling the octahedral holes within the close-packed anion
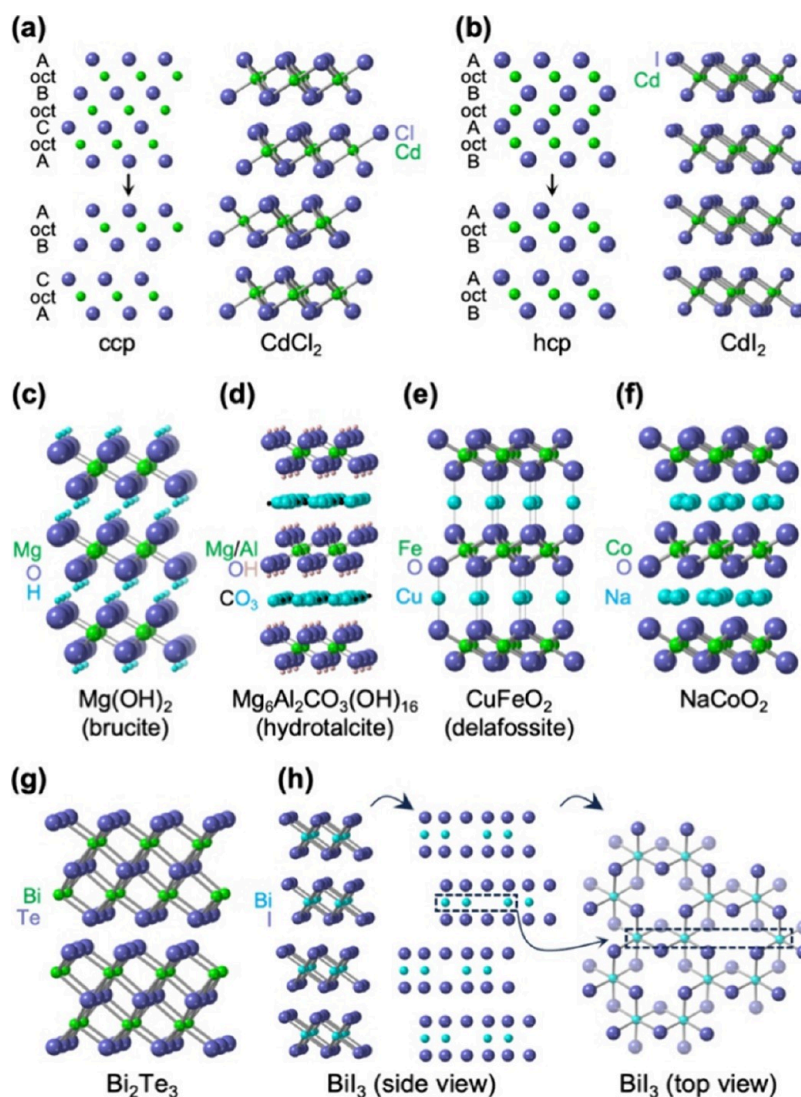
Figure 7. Layered structures derived from the rocksalt and NiAs structures. (a) Removing every other layer of cations from the rocksalt structure produces the CdCl$_2$ structure, while (b) removing every other layer of cations from the NiAs structure produces the CdI$_2$ structure. The CdCl$_2$ and CdI$_2$ structures are both van der Waals layered solids and differ only in the orientations of the octahedra and how the layers are stacked relative to one another. Several layered structures are derivatives of CdCl$_2$ and CdI$_2$, as shown in (c) through (f). (c) Brucite [e.g., Mg(OH)$_2$] is related to CdCl$_2$ but has two-atom OH$^-$ anions, with the hydrogen atoms located in the interlayer space. (d) Hydrotalcite [e.g., Mg$_6$Al$_2$CO$_3$(OH)$_{16}$] is related to brucite but with alternating orientations of the octahedral layers and carbonate anions between the layers. Water molecules are omitted for clarity. (e) Delafossite [e.g., CuFeO$_2$] and (f) NaCoO$_2$ have the same orientation of octahedral layers as hydrotalcite, but with copper (in linear coordination) or sodium (often with partial occupancy) cations between the anionic layers. (g) Bi$_2$Te$_3$ can be derived from rocksalt by removing every third layer of cations (relative to removing every other layer to derive CdCl$_2$). (h) BiI$_3$ is related to CdI$_2$ but with additional cation vacancies, in an ordered arrangement, within the octahedral layers, as shown in both the side and top views of the structure.

structure, we transform a 1:1 cation:anion ratio to a 0.5:1, or 1:2, cation:anion ratio. In doing so, we transform these three dimensionally bonded structures into two-dimensional structures with direct anion−anion contacts, i.e., van der Waals layered solids. The rocksalt-derived structure is CdCl$_2$ (Figure 7a) and the NiAs-derived structure is CdI$_2$ (Figure 7b). The only difference between these structures is the orientation of the octahedra and how the layers stack relative to each other which, again, is a consequence of differing anion close packing arrangement, i.e., ccp vs hcp. These are common precursors to 2D nanosheets. For example, PdTe$_2$, PtSe$_2$, TaS$_2$, and related "beyond-graphene" materials have CdI$_2$ structures that are distinct from the more common transition metal dichalcogenides MX_2 (M = Mo, W; X = S, Se, Te).[49−52]

The crystal structures of many layered hydroxides, including Fe(OH)$_2$, Co(OH)$_2$, Ni(OH)$_2$, and their solid solutions, adopt CdI$_2$-related structures. For example, Mg(OH)$_2$ crystallizes in the brucite structure (Figure 7c), which is a variant of CdI$_2$ that has OH$^-$ groups in place of each iodide anion. Layered double hydroxides, which are also commonly studied 2D nanoscale materials for catalysis and energy storage applications, are related to NiAs and CdI$_2$ as well, with additional anions between CdI$_2$-like metal hydroxide layers to compensate additional positive charge (Figure 7d). The delafossite structure type, typified by CuFeO$_2$, can be described as CdCl$_2$- or CdI$_2$-like layers of edge-sharing octahedra that are connected through linear bridges with other cations (Figure 7e). Na$_x$CoO$_2$, which functions as a superconductor,[53] a thermoelectric material,[54] and a cathode material for sodium ion batteries,[55] depending on
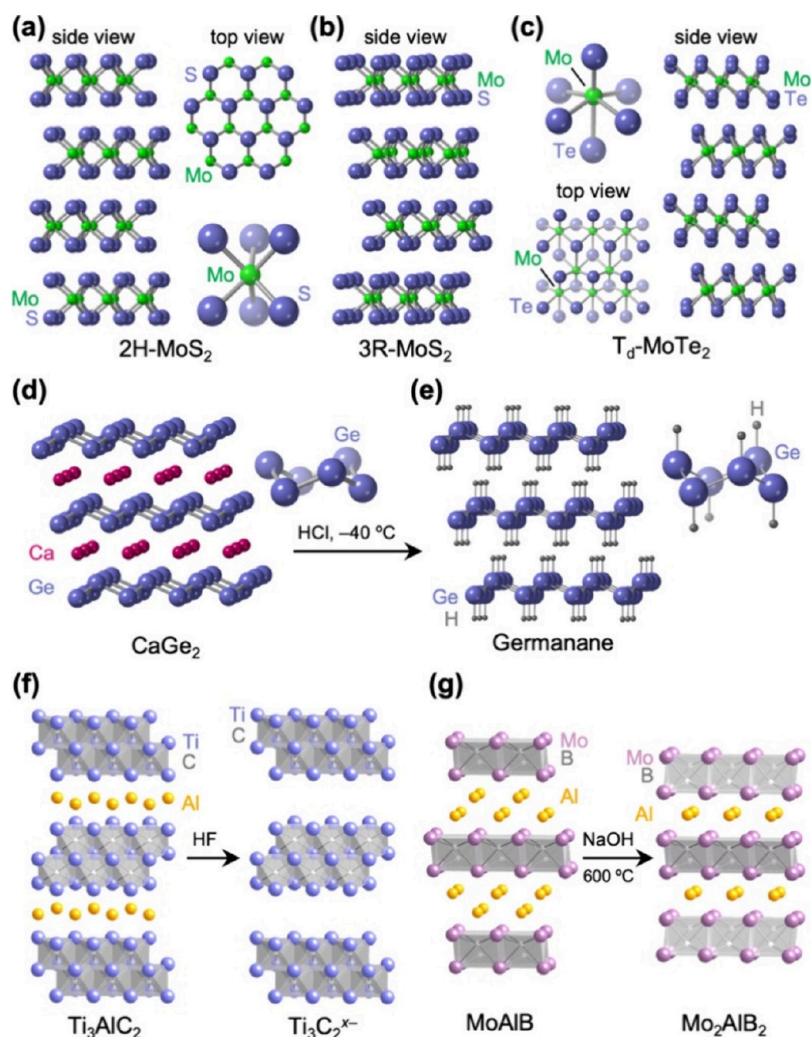
Figure 8. Structures and reactions of beyond-graphene layered materials. The layered transition metal dichalcogenides adopt several distinct structures that differ based on the coordination environments of the metal cations, the stacking arrangements of the metal–chalcogen layers, and the distortions of the metal–chalcogen polyhedra. Three examples are shown: (a) 2H-MoS$_2$, (b) 3R-MoS$_2$, and (c) T_d-MoTe$_2$. The structure of the layered intermetallic compound CaGe$_2$ is shown in (d), along with the structure of germanane (e), which retains the structure of the germanium layers upon topochemical deintercalation of the calcium. The structures of the prototypical MAX phase Ti$_3$AlC$_2$ and the prototypical MXene Ti$_3$C$_2^{x-}$ formed from deintercalation of the Al in Ti$_3$AlC$_2$ by HF are shown in (f). The structure of the stable MAB phase MoAlB and the metastable derivative Mo$_2$AlB$_2$, formed from deintercalating half of the Al from MoAlB with NaOH following by thermal crystallization, is shown in (g).

the value of x and the extent of hydration, has a similar CdCl$_2$-like structure with $[CoO_2]^{n-}$ layers interleaved with nNa$^+$ cations (Figure 7f). The crystal structure of Bi$_2$Te$_3$, a layered compound that is often studied as a nanostructured material for its thermoelectric properties[56] and as a topological insulator,[57] is derived from rocksalt by removing every third layer of cations. The resulting structure has rocksalt-like Bi$_2$Te$_3$ bilayers that are reminiscent of the CdCl$_2$ structure, along with direct Te–Te contacts (Figure 7g). BiI$_3$, a 2D material that has been studied for its topological properties,[58] has a crystal structure that is related to CdI$_2$, but with only two-thirds of the metal sites filled in each bismuth iodide layer (Figure 7h).

Transition metal dichalcogenides (TMDs), which include MoX_2 and WX_2 (X = S, Se, Te), are ubiquitous 2D nanomaterials because of their thickness-dependent electronic properties.[59] The TMDs adopt multiple polymorphs, which are different crystal structures for the same composition.[60] The structure of the most stable form of MoS$_2$ is hexagonal and is referred to as 2H-MoS$_2$; "H" refers to its hexagonal unit cell and "2" refers to the stacking sequence. MoS$_2$ and other TMDs are

not close packed structures because they include eclipsed layers, but the way in which we have been viewing close packed structures is also helpful for understanding the TMD structures. Figure 8a shows two views of the 2H-MoS$_2$ crystal structure. The side view shows a nominal ABABAB stacking sequence of MoS$_2$ layers, which corresponds to a stacking sequence of AABBAABB for the sulfur anion layers. The top view shows a hexagonal arrangement of sulfur anions. The molybdenum cations are sandwiched between eclipsed triangles of sulfur anions, leading to a trigonal prismatic coordination environment. Figure 8b shows the side view of the triple-layer rhombohedral polymorph, 3R-MoS$_2$, which has a nominal ABCABC stacking sequence of MoS$_2$ layers that also have trigonal prismatic coordination of molybdenum cations by sulfur anions. MoS$_2$ and the other TMDs have additional polymorphs as well. 1T-MoS$_2$ is trigonal and has eclipsed MoS$_2$ layers with octahedral coordination. 1T'-MoS$_2$ is related to 1T-MoS$_2$ but with the cations forming dimers, which creates a distorted zigzag arrangement of Mo atoms that also results in a slight shift of the anions. T_d-MoTe$_2$, shown in Figure 8c, has octahedral coordination with staggered layers
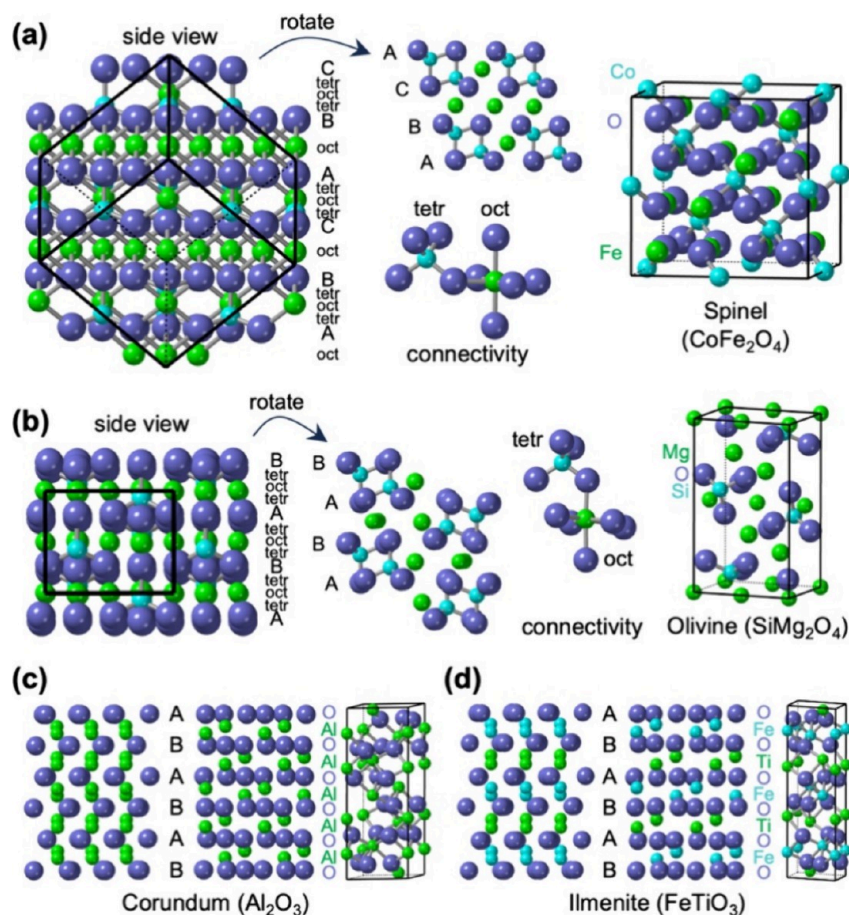
Figure 9. Structures derived from mixed partial occupancy of both octahedral and tetrahedral sites. Derivations of (a) the spinel structure from systematic filling by cations of half of the octahedral holes and one-eighth of the tetrahedral holes in ABCABC (ccp) close-packed layers and (b) the olivine structure by the same fractional filling of octahedral and tetrahedral holes as spinel, except for ABAB (hcp) close-packed layers. In both (a) and (b), two views of the close-packed layers and the filled holes are shown, along with the connectivities that highlight how the tetrahedra and octahedra are oriented relative to one another. The unit cells for spinel-type $CoFe_2O_4$ and olivine-type $SiMg_2O_4$ (often written as Mg_2SiO_4) are also shown. The result of filling two-thirds of the octahedral holes with Al^{3+} cations in close-packed ABAB (hcp) layers of O^{2-} anions forms the corundum structure, shown for Al_2O_3 in (c). Analogous filling but with two different cations that alternate in layers forms the ilmenite structure, shown for $FeTiO_3$ in (d). For (c) and (d), two views plus the unit cell are presented.

similar to 2H-MoS$_2$, but the distorted octahedra lead to staggered chalcogen layers on either side of the metal in T_d-MoTe$_2$, which is in contrast to the eclipsed chalcogen layers in 2H-MoS$_2$.

The MoS$_2$ system provides an instructive example of how a fundamental structural building block, in this case S−Mo−S layers, can arrange in different ways (including different coordination environments and different stacking sequences) to generate multiple distinct crystal structures that each have unique properties. Identifying and understanding these structural relationships is important in nanoscale systems because it can provide clues about how to design and access new nanomaterials. For example, the exceptional and unique thickness-dependent properties of graphene,[61] which consists of atomically thin 2D sheets of graphite-like carbon, have led to interesting 2D nanosheet analogues of other metallic and semiconducting elements and components, including germanium (germanene),[62] phosphorus (phosphorene),[63] boron (borophene),[64] metal carbides and nitrides (MXene),[65] and metal borides (MBene[66] or boridene[67]). Moving from theoretical interest to experimental realization requires synthesizing these and other 2D materials. One prominent pathway to such 2D materials involves topochemical manipulations, which

modify composition and local structure while maintaining an overall extended structural framework.[68−71] This strategy requires the identification of a crystal structure that contains the desired 2D material as a subunit, and then the development of a synthetic pathway to isolate this subunit from the other parts of the crystal.

The intermetallic compound CaGe$_2$ is an example of a parent structure that may be amenable to a topochemical transformation to a 2D material. CaGe$_2$ (Figure 8d) contains alternating layers of calcium and buckled sheets of germanium having a chair-type conformation similar to what we discussed as a key building unit of the hexagonal wurtzite structure in Figure 5n. Reacting CaGe$_2$ with hydrochloric acid at temperatures as low as −40 °C results in topochemical deintercalation of Ca, i.e., the removal of calcium without disrupting the germanium layers (Figure 8e).[62] Concomitant with the deintercalation of Ca, hydrogen adds to the germanium, ultimately forming 2D sheets of germanane, GeH, which is a germanium analogue of graphane that is formed upon hydrogenation of graphene; the local structure (chair conformation) is retained. Other prominent examples where the identification of structural relationships lead to the synthesis of new classes of nanomaterials include MXenes (Figure 8f), which form from the topochemical deintercalation
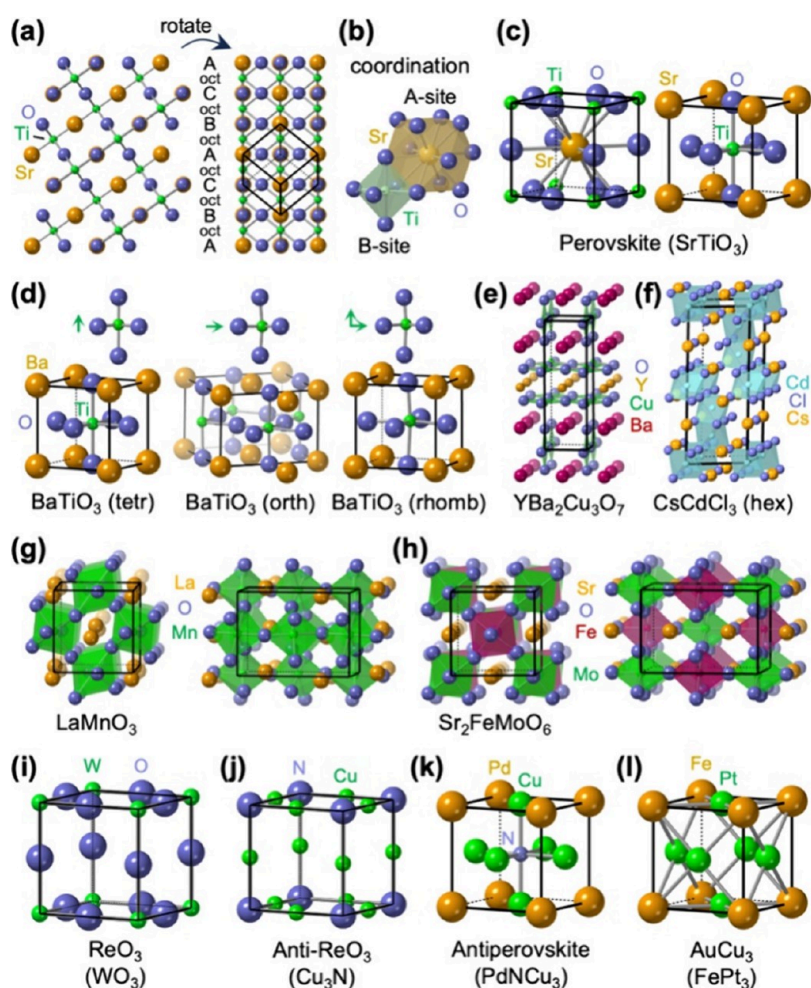
Figure 10. Perovskite and perovskite-related crystal structures. (a) Derivation of the perovskite structure by systematically filling one-quarter of the octahedral holes in ABCABC (ccp) close packed layers with cations, and replacing one-third of the anions with cations. A perovskite unit cell is indicated within the rotated view of the structure. The coordination environments of the A-site and B-site cations are shown in (b). Two unit cells for the cubic perovskite $SrTiO_3$ are shown in (c); one centers the A-site cation (Sr^{2+}) and the other centers the B-site cation (Ti^{4+}). In addition to a cubic perovskite structure, $BaTiO_3$ adopts tetragonal, orthorhombic, and rhombohedral variants to capture various distortions of the Ti−O octahedra, as indicated by the green arrows (d). Crystal structures are also shown for the perovskite-related compounds (e) $YBa_2Cu_3O_7$ and (f) $CsCdCl_3$. The structure of $CsCdCl_3$ (and similar compounds) is often referred to as a hexagonal perovskite. $LaMnO_3$ is an example of a perovskite that exhibits cooperative distortion (tilting) of the octahedra, as shown in (g). Similar cooperative distortions, coupled with checkerboard-type cation ordering, is observed in the double perovskite Sr_2FeMoO_6, shown in (h). Unit cells are also shown for the perovskite-derived structures of (i) ReO_3 (e.g., WO_3), (j) anti-ReO_3 (e.g., Cu_3N), (k) antiperovskite (e.g., $PdNCu_3$), and (l) $AuCu_3$ (e.g., $FePt_3$).

of Al from metal aluminum carbides or nitrides (MAX phases) such as Ti_3AlC_2,[72] and MBenes (or boridenes), which form from the topochemical deintercalation of Al from substituted metal aluminum borides (MAB phases) such as $(Mo_{2/3}Y_{1/3})_2AlB_2$.[67] Related partial deintercalation processes can lead to the formation of metastable phases, such as the removal of half of the Al from MoAlB to form $MoAl_{0.5}B$, or Mo_2AlB_2 (Figure 8g), which has only been synthesized through topochemical methods.[73,74]

Our preceding discussion of the crystal structures of several prominent classes of 2D nanomaterials provides an opportunity to address a few common misconceptions. For example, it is sometimes incorrectly assumed that all MX_2 compounds, where M is a transition metal or post-transition metal, are layered van der Waals solids, given the prominence of TMDs. While MoX_2 and WX_2 (X = S, Se, Te) are certainly layered van der Waals solids, some TMDs are three dimensionally bonded structures. For example, FeS_2, CoS_2, and some other 3d transition metal dichalcogenides adopt the pyrite structure, which was shown in

Figure 3j as a derivative of rocksalt. To be a layered van der Waals solid would require S^{2-} anions and M^{4+} cations, which are not chemically reasonable options for these elements, where the metals would prefer to be M^{2+} and the sulfur anions compensate charge by forming the S_2^{2-} dimer. The monochalcogenides SnS, SnSe, GeS, and GeSe also are sometimes referred to as van der Waals layered solids, but as is shown in Figure 3k, they too adopt a distorted variant of the rocksalt structure. The crystal structure certainly has layered character and crystals typically grow as plates that reflect the differences in bonding laterally vs vertically. However, van der Waals structures typically have metal cations sandwiched *between* layers of anions, such that only the anions are exposed, and in contact, within the interlayer region. For the tin and germanium monochalcogenides, as rocksalt derivatives, the cations also occupy sites in the same plane as the anions (even considering the slight distortions), and therefore are partially exposed in the interlayer region and help to compensate the charge of the anions. These structural details are important to recognize when analyzing the nature of the

bonding and interpreting the properties of dimensionally confined nanomaterials.

CLOSE-PACKED STRUCTURES OF MIXED-METAL COMPOUNDS

We began by considering how the systematic filling of various octahedral and tetrahedral holes in close packed lattices allowed us to derive a large number of distinct, but related, crystal structures. We then diverged to consider derivative layered structures formed from removing atoms in certain locations. Here we return to the approach of building structures by considering additional motifs that can be generated through systematic partial filling of various types of holes. If we fill only half of the octahedral holes and one-eighth of the tetrahedral holes in a ccp anion lattice, we derive the spinel structure (Figure 9a), which is commonly observed among prominent types of magnetic and catalytic oxide and sulfide nanoparticles.[75−77] Using oxides as the prototypical examples, spinels have a formula of AB_2O_4, where A corresponds to tetrahedrally coordinated cations and B corresponds to octahedrally coordinated cations. The connectivities of the octahedra and tetrahedra within the spinel structure are shown in Figure 9a. Energetic considerations, which will not be addressed here, help to rationalize which cations prefer to be in which sites and whether the spinel is classified as "normal" or "inverse". The most common oxide spinel nanoparticles are the ferrites,[78] such as $CoFe_2O_4$, or more generically MFe_2O_4, which have one M^{2+} cation along with two Fe^{3+} cations per formula unit. The same element, in a mix of 2+ and 3+ oxidation states, can comprise all of the cation sites in the spinel. For example, spinel-type Fe_3O_4 (magnetite) is a ubiquitous magnetic material, and Fe_3O_4 nanoparticles are used frequently in magnetic resonance imaging[79] and as the steerable components of active nanostructures.[80] Nanoparticles of isostructural spinel Fe_3S_4 (greigite) have been explored as catalysts,[81] especially since Fe_3S_4 contains iron sulfur clusters that are structurally related to those found in many enzymes. For completeness, we note that analogous filling of holes — half of the octahedral holes and one-eighth of the tetrahedral holes — but in a hcp anion lattice (instead of ccp as in spinel) leads to the olivine structure (Figure 9b). The unit cell for the olivine structure looks quite different from the unit cell for the spinel structure, but the ways in which the structures are derived, as well as the connectivities of the octahedra and tetrahedra, are related to one another, as can be seen by comparing Figures 9a and 9b.

Filling two-thirds of the octahedral holes in a hcp anion lattice forms the corundum structure (Figure 9c), which is adopted by Al_2O_3 that is used as an insulating layer in nanoelectronic devices[82] and Fe_2O_3 that is studied as a material for solar absorption and photocatalysis.[83] Filling two-thirds of the octahedral holes in a hcp anion lattice in an ordered arrangement leads to the ilmenite structure (Figure 9d), which has the same M_2O_3 composition but with alternating cations, i.e., $M^IM^{II}O_3$. $FeTiO_3$ is a common ilmenite-type compound that has been explored at the nanoscale as both a magnetic[84] and a catalytic[85] material.

The structures in Figure 9 highlight several important points that are useful to consider when viewing and comparing crystal structures. First, unit cells that seem complex, with a large number of atoms in locations that do not appear related or systematic at first glance, can relate to simpler structures that are easier to understand based on how they are derived. Second, structures that seem, from their unit cells, to be unrelated to one

another can indeed be closely related, when one considers aspects of local structure and connectivity, as well as how they are derived. Finally, structures that have cations (or anions) of the same element but in distinct crystallographic sites can be related to structures having cations (or anions) of different elements, despite looking different because of how the cations (or anions) are ordered.

PEROVSKITE AND PEROVSKITE-DERIVED CRYSTAL STRUCTURES

Replacing one-third of the anions in a ccp anion lattice with a cation while also filling one-fourth of the octahedral holes, both in an ordered arrangement, generates the perovskite structure (Figure 10a), which, like ilmenite, also has a $M^IM^{II}X_3$ composition.[86] Perovskite-structured materials include mixed metal oxides,[87] halides,[88,89] chalcogenides,[90] mixed-anion compounds,[91] intermetallic compounds,[92] and hybrid organic/inorganic systems,[93] making them one of the most versatile and studied classes of materials. As nanoscale materials, perovskite-structured compounds are widely used as catalysts and solar materials.[94]

In the general perovskite formula of $M^IM^{II}X_3$, M^I corresponds to the "A-site" cation, which has a coordination number of 12, while M^{II} corresponds to the "B-site" cation, which sits at the center of an octahedron that coordinates it to six X anions. These coordination environments are shown in Figure 10b. Figure 10c shows two distinct unit cells for perovskite, each emphasizing different aspects of the structure. One unit cell emphasizes the cubic network of corner-sharing octahedra by placing the smaller B-site cations at the corners, bridged by the X anions, with the larger A-site cations at the center of each cube. The other unit cell emphases the octahedral coordination of the B-site cation by placing it at the center of an octahedron formed by six X anions, with the A-site cations in the corners.

It is common for the octahedra in the perovskite structure to be distorted relative to an ideal octahedron that has one atom at the center and six equidistant atoms surrounding it. $BaTiO_3$, for example, can exist in several different polymorphs, which are stable under different conditions. The key differences among the structures involve the symmetry of the octahedron, which changes the symmetry of the unit cell. Figure 10d shows the tetragonal, orthorhombic, and rhombohedral unit cells that exist for the various polymorphs of $BaTiO_3$, in addition to a cubic unit cell like that of $SrTiO_3$ shown in Figure 10c.[95] The corresponding octahedra are also shown, highlighting how the central Ti^{4+} cation displaces in various ways (indicated by the green arrows next to the octahedra) as the symmetry decreases. These subtle structural differences are important, as they lead to different electrical properties for $BaTiO_3$. As is evident for the orthorhombic $BaTiO_3$ cell, sometimes larger unit cells are required to capture the symmetry of the distorted octahedra. In addition to distortions, both the A and B sites can accommodate mixtures of cations, which can arrange either randomly in a solid solution or in various ordered motifs. For example, the ubiquitous copper oxide superconductor $YBa_2Cu_3O_7$ (or $Y_{1/3}Ba_{2/3}CuO_{2.33}$) can be thought of as a triple-layer perovskite (with oxygen vacancies) that has Cu in all of the B sites and an alternating arrangement of Ba, Ba, and Y layers in the A sites (Figure 10e).[96]

Here, it is important to recognize the formal differences between perovskite and nonperovskite structures that are related to or derived from perovskite, but that are nonetheless distinct.[97,98] Many experts prefer to save the designation of
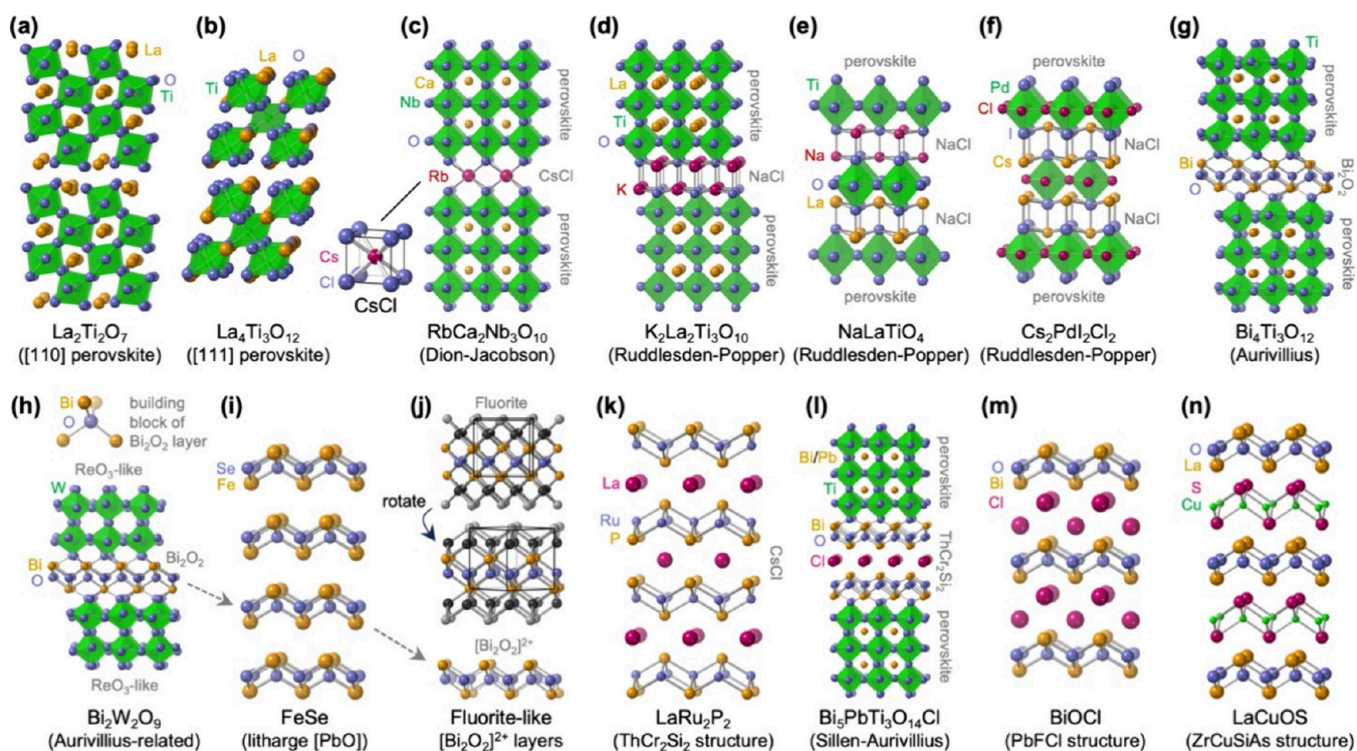
Figure 11. Representative examples of layered and intergrowth structures. (a) $La_2Ti_2O_7$ and (b) $La_4Ti_3O_{12}$ are examples of layered perovskites formed by cutting and then stacking the perovskite structure along the [110] and [111] directions, respectively, while the layered perovskites in (c) through (h) form by cutting and then stacking the perovskite structure along the [100] direction. Three common classes of [100] layered perovskites are the (c) Dion-Jacobson, (d–f) Ruddlesden−Popper, and (g–h) Aurivillius phases. Dion-Jacobson phases can be described as an intergrowth of CsCl-like layers with perovskite layers, which can vary in thickness; a three-layer phase, $RbCa_2Nb_3O_{10}$, is shown in (c). The unit cell for the CsCl structure is shown for comparison. Ruddlesden−Popper phases can be described as intergrowths of rocksalt (NaCl) and perovskite layers. The three-layer Ruddlesden−Popper phase $K_2La_2Ti_3O_{10}$ is shown in (d), along with the single-layer Ruddlesden−Popper phase $NaLaTiO_4$, with ordered alternating Na^+ and La^{3+} cations, in (e) and the single-layer mixed-anion halide Ruddlesden−Popper phase, with ordered I^- and Cl^- anions, in (f). Aurivillius phases, such as $Bi_4Ti_3O_{12}$ in (g), are intergrowths of anionic perovskite layers $[(Bi_2Ti_3O_{10})^{2-}]$ and cationic bismuth oxide $[(Bi_2O_2)^{2+}]$ layers. $Bi_2W_2O_9$, shown in (h), has distorted ReO$_3$-like layers with vacant A-sites relative to perovskite. The $(Bi_2O_2)^{2+}$ unit, which is the building block for the bismuth oxide layers, is also shown in (h). Litharge-type PbO has an analogous structure to that of the $(Bi_2O_2)^{2+}$ layers in the Aurivillius phases; the structure of PbO-type FeSe is shown in (i). The structure of these $(Bi_2O_2)^{2+}$-like layers can be extracted from the fluorite structure, as shown in (j). When these fluorite-like layers interleave with cations as shown for $LaRu_2P_2$ in (k), the $ThCr_2Si_2$ structure emerges. The foundational structural unit of $ThCr_2Si_2$ can interleave with perovskite to form Sillen-Aurivillius phases such as $Bi_5PbTi_3O_{14}Cl$ shown in (l). When the $(Bi_2O_2)^{2+}$-like layers instead interleave with a zigzag double layer of anions, mixed-anion phases emerge, such as PbFCl-type BiOCl in (m). Replacing the interlayer Cl^- in LaOCl (which has the same structure as BiOCl) with $[CuS]^-$ layers forms (n) LaCuOS (or LaOCuS), an intergrowth of $[LaO]^+$ and $[CuS]^-$.

"perovskite" for true ABX_3 perovskites, but there are different perspectives among different researchers. For example, so-called hexagonal perovskites (Figure 10f) have face-sharing BX_3 octahedra and therefore lack the corner-shared octahedral network that defines true perovskites. Nevertheless, the fundamental building block of a hexagonal perovskite is closely related to that of a cubic perovskite in terms of the distribution of atoms placed on the lattice.[99]

$BaTiO_3$ provided a useful example of various distortions of the octahedra that are possible by shifting the position of the central metal B-site cation. Distortions can also arise from the influence of the B-site cations. For example, in $LaMnO_3$,[100] the manganese oxide octahedra tilt cooperatively to maximize interactions with the B-site La^{3+} cation (Figure 10g). The result is a highly distorted zigzag tilting pattern relative to the ideal perovskite structure. Additionally, the presence of multiple cations can induce ordered arrangements, particularly when the cations have different sizes and/or charges. For example, Sr_2FeMoO_6[101] is a "double perovskite" (relative to the formula $SrFe_{0.5}Mo_{0.5}O_3$) that contains Sr^{2+} on all A-sites but a mixture of Fe^{2+} and Mo^{6+} on the B-sites. The very different charges of the Fe^{2+} and Mo^{6+}

cations help to facilitate their ordering in a 3D checkerboard motif that resembles the alternating cation/anion structure of rocksalt (Figure 10h). Sr_2FeMoO_6 adopts a structure having tilted octahedra that is similar to that of $LaMnO_3$ in Figure 10g, but with the added B-site cation ordering. Double perovskites can also order the B-site cations in alternating layers instead of a rocksalt-type motif, as well as have A-site ordering. Triple and quadruple perovskites are also known, as are mixed-anion perovskites with anion ordering, such as $SrTaO_2N$.[102]

We now consider several broader classes of perovskite-related and perovskite-derived structures. These are structures that one can view as starting from perovskite but with systematic modifications that lead to distinct structures.[103] As a first example, removing the A-site cations from the nondistorted perovskite structure of $SrTiO_3$ produces the ReO_3 structure (Figure 10i), which can be described as a 3D network of corner-sharing octahedra. ReO_3-type oxides are commonly observed as nanostructured materials such as WO_3, which is used as a catalyst support and for its electrochromic properties upon electron injection.[104,105] Note that certain metals, such as Li or Rb, can be reductively inserted into the empty A sites of certain

redox-active ReO_3-structured oxides. However, this insertion reaction typically results in a significant structural change, such as a shift to a hexagonal tungsten bronze, as is the case for $Rb_{0.33}WO_3$.[106] The anti-ReO_3 structure (Figure 10j) switches the cation and anion positions of ReO_3. A common example is Cu_3N, which is often synthesized as nanoparticles that are active catalysts for the oxygen reduction reaction.[107] Anti-ReO_3-type Cu_3N has copper octahedra with nitrogen at the center. The vacant A-sites can be filled with Pd to form $PdNCu_3$ (more commonly written as Cu_3PdN), which can also be made as nanoparticles.[108,109]

$PdNCu_3$ is an example of an antiperovskite structure (Figure 10k), which still maintains the formula of perovskite, ABX_3. The antiperovskite structure can be adopted by mixed metal carbides, borides,[92] nitrides,[110] phosphides,[111] and suboxides.[112] (In contrast to oxides, which are typically oxygen-rich with oxygen defining the lattice in which smaller interstitial metals reside, suboxides are metal-rich with oxygen located in interstitial sites.[113,114]) Rather than having a small-sized metal sit in the B-site surrounded by an octahedron of larger anions, which is the case for perovskite, the octahedron in antiperovskite is composed of a metal and the B-site contains carbon, boron, nitrogen, phosphorus, oxygen, etc. Essentially, the positions of the metals and the anions are switched in antiperovskite relative to perovskite. The A-site cation is then a more electropositive metal. Examples of antiperovskites beyond $PdNCu_3$ include superconducting $MgCNi_3$[115] and superionic conducting $ClOLi_3$.[116] The $AuCu_3$ structure, which is common among intermetallic alloy nanoparticles of interest for catalysis and magnetic information storage depending on their constituent elements,[117,118] can be thought of as the antiperovskite structure without the central B-site element (Figure 10l).

Other prevalent classes of perovskite-related compounds are classified as layered perovskites. In layered perovskites, the cubic perovskite structure is truncated along certain crystallographic directions and stacked vertically and/or interleaved with other cations or structural units. For example, cutting a perovskite along the [110] direction generates a layered perovskite such as $La_2Ti_2O_7$[119] (Figure 11a), and cutting perovskite along the [111] direction generates a layered perovskite such as $La_4Ti_3O_{12}$[120] (Figure 11b). Among the most common layered perovskites are those that result from cutting along the [100] direction and inserting another structural unit between the resulting perovskite slabs, which typically range in thickness from one to three perovskite units but can be thicker in some cases. If the perovskite layers are eclipsed and interleaved with a cation that is lined up with the A-site cations, a class of layered perovskite called a Dion-Jacobson[121,122] (DJ) phase emerges (Figure 11c). A Dion-Jacobson phase can be thought of as an intergrowth of the perovskite and CsCl structures. (The CsCl structure, which is related to bcc in Figure 1s but with different elements at the center versus in the corner, is also shown in Figure 11c.) Dion-Jacobson phases have a general formula $AA'_{n-1}B_nO_{3n+1}$, where n corresponds to the number of cubic perovskite units that comprise the perovskite slabs; $RbLaNb_2O_7$ is a n = 2 phase and $RbCa_2Nb_3O_{10}$ is a n = 3 phase.

If the perovskite slabs are instead staggered and interleaved with twice the number of cations per perovskite unit and in a staggered motif, the Ruddlesden−Popper[123,124] (RP) family of layered perovskites emerges (Figure 11d). Ruddlesden−Popper phases, which can be thought of as an intergrowth of the perovskite and rocksalt structures, have a general formula of $A_2A'_{n-1}B_nO_{3n+1}$; $K_2CaTa_2O_7$ is a n = 2 phase and $K_2La_2Ti_3O_{10}$ is

a n = 3 phase. Using A cations having significantly different charges can lead to ordering, as is observed for the n = 1 Ruddlesden−Popper phase $NaLaTiO_4$ (Figure 11e). As was discussed earlier for 2D materials, many of these layered perovskites can be topochemically manipulated and exfoliated to produce 2D oxide nanosheets.[69] In addition to oxides, there are many examples of halide perovskites and hybrid organic−inorganic perovskites that adopt these layered structures, including $(3AMP)(MA)_3Pb_4I_{13}$ [3AMP = 3-(aminomethyl)-piperidinium, MA = methylammonium],[125] a n = 4 Dion-Jacobson phase, and $Cs_2PbI_2Cl_2$[126] (Figure 11f) a n = 1 Ruddlesden-popper phase with ordered iodide and chloride anions.

■ INTERGROWTH STRUCTURES

Beyond the layered perovskites discussed above, other families of layered and intergrowth compounds are also common and frequently encountered in nanoscale systems. We begin by considering structures derived by interleaving perovskite slabs with other structural units. Intergrowths of perovskite and bismuth oxide are called Aurivillius[127] phases (Figure 11g) and have the general formula $Bi_2O_2−A_{n-1}B_nO_{3n+1}$. A representative n = 3 Aurivillius phase is $Bi_4Ti_3O_{12}$, or $(Bi_2O_2)Bi_2Ti_3O_{10}$, with Ti occupying the B sites and Bi occupying the A sites, as well as within the bismuth oxide layers. Note that for these layered perovskites, the perovskite slabs are negatively charged while the interlayer cations or structural units compensate with positive charge. In the case of $Bi_4Ti_3O_{12}$, the bismuth oxide layers are $[Bi_2O_2]^{2+}$ while the perovskite layers are $[Bi_2Ti_3O_{10}]^{2-}$. $Bi_2W_2O_9$, shown in Figure 11h, is an example of an n = 2 Aurivillius-like phase. $Bi_2W_2O_9$ can be thought of as an intergrowth of bismuth oxide and a distorted ReO_3-like structure, i.e., perovskite-like layers without A-site cations.

The bismuth oxide layers in Aurivillius phases have a zigzag metal-anion arrangement, with planar layers of anions (i.e., oxide) that are tetrahedrally coordinated to four cations (i.e., bismuth) − two above and two below (Figure 11h). The crystal structure of α-PbO, litharge, is composed entirely of such layers, as shown for FeSe[128] in Figure 11i. This motif is related to layers that appear in the fluorite structure (initially shown in Figure 5g); a comparison is shown in Figure 11j. These extended tetrahedrally coordinated metal−anion zigzag layers, with the general formula $[M_2X_2]^{2+}$, are a common building block of many types of intergrowth structures. If we interleave these fluorite-like $[M_2X_2]^{2+}$ layers with CsCl-like layers of cations, we get the $ThCr_2Si_2$ structure, which is so commonly observed and versatile that it has been described as the "perovskite of intermetallic compounds".[129] One example, shown in Figure 11k, is $LaRu_2P_2$,[130] a superconducting metal phosphide phase. If we begin with an Aurivillius phase, which is an intergrowth of perovskite and bismuth oxide, and interleave the perovskite layers with layers that are structurally related to $ThCr_2Si_2$ (but reversing the positions of the anions and cations), we get a family of Sillen-Aurivillius[131] phases that include compounds such as $Bi_5PbTi_3O_{14}Cl$ (Figure 11l).

We now focus on the bismuth oxide layers in the Aurivillius phases, which as isolated slabs can be described as $[Bi_2O_2]^{2+}$ that is charge compensated by the anionic perovskite layers. Using these $[Bi_2O_2]^{2+}$ subunits as the primary building block, we can derive structures like $BiOX$[132] and $LaOX$[133] (X = F, Cl, Br, I). These layered compounds have analogous oxide layers — $[Bi_2O_2]^{2+}$ in $BiOX$ and $[La_2O_2]^{2+}$ in $LaOX$ — that are interleaved and charge compensated by double layers of halide
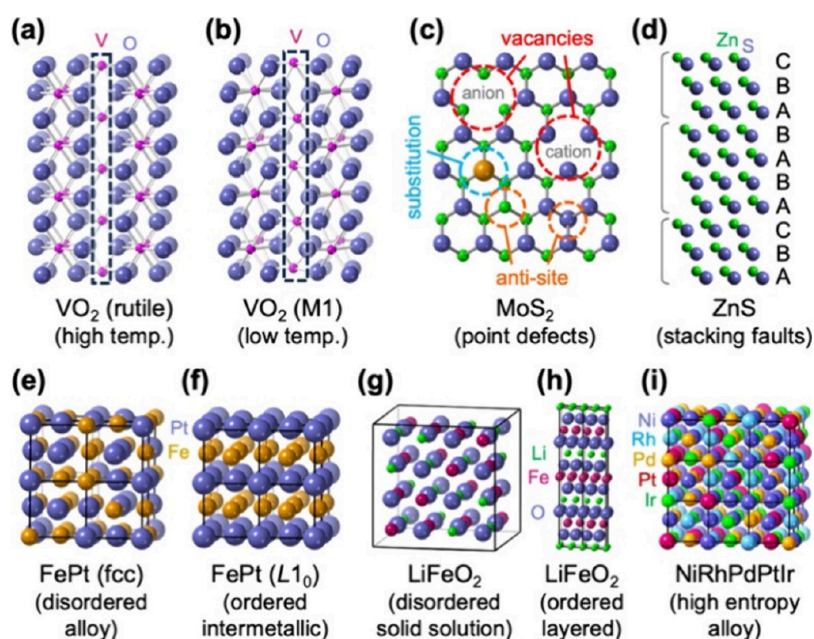
Figure 12. Examples of structural distortions, defects, stacking faults, and disordered vs ordered structures. Crystal structures are shown for the (a) high temperature (rutile) and (b) low temperature (M1) phases of VO_2. The dashed boxes highlight the chains of vanadium atoms, which are equally spaced in (a) and staggered with alternating shorter and longer bond lengths in (b). A single planar layer of MoS_2 is shown in (c), along with various types of point defects; anion and cation vacancies are circled in red, a substitutional defect is circled in blue, and antisite defects are circled in orange, as indicated. Stacking faults in ZnS are depicted in (d) with alternating regions of ABC and AB stacking sequences of the close-packed planes of sulfur anions. The crystal structures (with multiple unit cells highlighted) of FePt corresponding to (e) disordered fcc alloy and (f) ordered $L1_0$ intermetallic forms having the same compositions are shown. Similarly, the crystal structures of $LiFeO_2$ corresponding to (g) a disordered rocksalt-like solid solution and (h) an ordered layered phase are also shown. A structural depiction of the five-metal high entropy alloy NiRhPdPtIr, which adopts a face centered cubic structure, is shown in (i).

anions (Figure 11m). As nanoparticles, BiOX compounds are widely studied as photocatalysts[134] while LaOX compounds are photoluminescent.[135] The α-PbO structure, discussed above and shown in Figure 11i, is generated by removing the interlayer halide anions in LaOX and BiOX, concomitant with reducing the charge on the cation from 3+ to 2+. As nanoparticles, each halide anion in LaOX can be replaced by a $[CuS]^-$ unit, transforming LaOX to LaOCuS (or LaCuOS), a layered intergrowth of lanthanum oxide and copper sulfide (Figure 11n).[136]

The intergrowth structures and their structural relationships highlighted in Figure 11 incorporate two primary subunits: perovskite layers and fluorite-like $[Bi_2O_2]^{2+}$ layers. Our focus was on showcasing how different and more complex structures can be derived from combining, in different arrangements, simpler structures we considered earlier. Many types of intergrowth compounds exist, and while our focus was on this small subset, the approach to viewing and comparing structural subunits is general and can be applied to many other classes of compounds as well.

FUNCTIONAL IMPACT OF SUBTLE STRUCTURAL AND COMPOSITIONAL DETAILS

The discussion above focused on how various crystal structures are derived, related, and visualized. Now, we turn to what one could consider to be more subtle variations in structure and composition in existing crystal structures that can profoundly impact their properties, particularly in nanoscale systems. While there are many relevant examples, here we focus on structural distortions, defects, and structural ordering vs disordering, as

well as some examples that demonstrate the important interplay between crystal structure and properties.

We begin with examples of structural distortions. During our discussion of perovskites, we already highlighted different distortions that can occur within or among the interconnected octahedra that define the structure (Figure 10d,g). These distortions can give rise to useful properties, including ferroelectricity and piezoelectricity, that result from cations that are moved off-center in the octahedra. Another example that is especially relevant among nanoscale systems is VO_2[137] (Figure 12a). Above 340 K, VO_2 adopts a rutile structure, with regularly spaced V^{4+} cations sitting at the center of each oxide octahedron, as highlighted by the dashed box. However, below 340 K, the rutile structure distorts such that the V^{4+} cations form pairs with alternating short and long V−V distances (Figure 12b). The distorted structure is semiconducting while the rutile structure is metallic, leading to a metal-to-semiconductor transition that is accompanied by changes in the optical and thermal properties as well.[138]

Like distortions, defects can have a similar impact on properties. As an example, Figure 12c shows various point defects that occur in TMD monolayers such as MoS_2. These point defects include vacancies on anion or cation sites and substitutions of atoms in the structure with different atoms in the compound that would not normally be at that site (antisite defects) or with different atoms not originally in the compound (substitutional defects). Such defects in TMDs can cause changes in the photoluminescence spectra, define the electrical transport behavior, induce magnetic ordering, and modify catalytic activity and/or selectivity.[139,140] Other types of defects, including planar defects, line defects, stacking faults, and grain
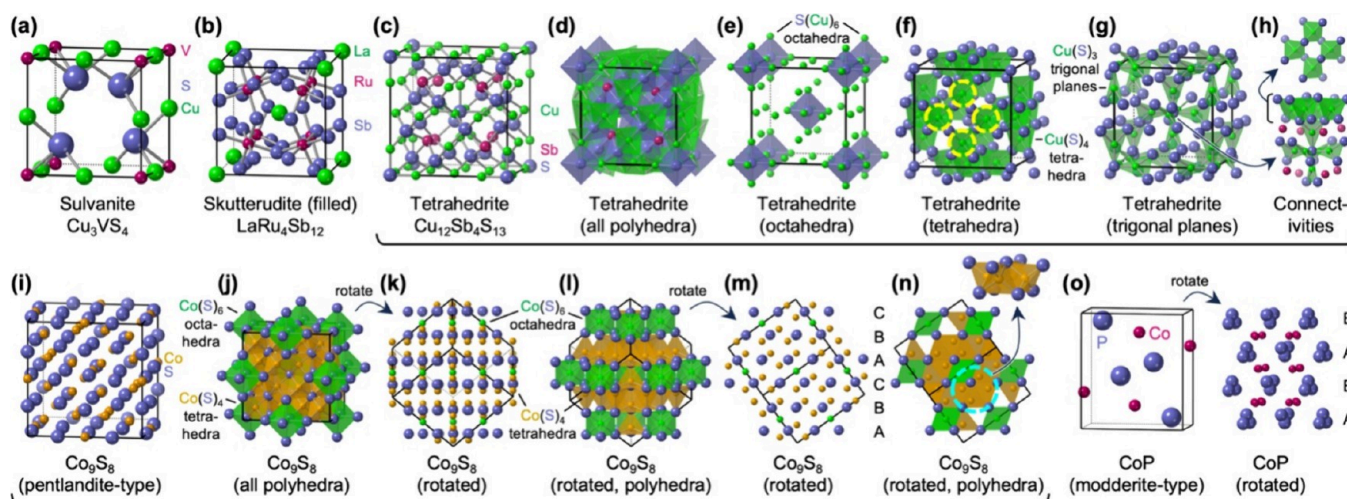
Figure 13. Crystal structures of compounds having greater compositional and/or structural complexity. Unit cells are shown for (a) sulvanite Cu_3VS_4, (b) filled skutterudite $LaRu_4Sb_{12}$, (c−h) tetrahedrite $Cu_{12}Sb_4S_{13}$, (i−n) pentlandite-type Co_9S_8, and (o) modderite-type CoP. For tetrahedrite $Cu_{12}Sb_4S_{13}$, in addition to the unit cell in (c), unit cells are also shown that emphasize (d) all polyhedra, (e) octahedra, (f) tetrahedra, and (g) trigonal planes. In (f), four tetrahedra, which comprise the center of a face of the unit cell, are highlighted in yellow dashed circles; this group of four tetrahedra are also shown at the top of (h), along with the connectivities of the polyhedra to each other. For pentlandite-type Co_9S_8, in addition to the unit cell in (i), unit cells are also shown in different orientations in (j), (l), and (n) that emphasize all polyhedra, along with corresponding unit cell rotations in (k) and (m) to emphasize the ABCABC close-packed layers. The inset in (n) highlights four interconnected tetrahedra (at the location highlighted by the blue dashed circle) that result in close metal−metal contacts. For modderite-type CoP, the unit cell is shown in (o), along with an expanded and rotated version of the structure to highlight the pseudoclose-packed ABAB layers of zigzag linear chains of phosphorus atoms.

boundaries, can similarly influence properties.[139,140] Figure 12d shows stacking faults in ZnS, which can be viewed as a random intergrowth of ABAB vs ABCABC stacking sequences of the close-packed layers.[42] Related stacking faults are commonly observed in semiconductor nanoparticles, including nanowires of II−VI, III−V, and group IV materials.[141]

We now turn from structural distortions and defects to various aspects of structural order vs disorder. Here, we are not considering amorphous materials, which have no long-range ordering, but rather crystalline materials that have various ways of arranging atoms on the lattice sites. The atomic-scale ordering vs disordering of various atoms in a crystalline alloy provides many prevalent examples among nanoscale materials systems. Mixing two or more atoms randomly on a crystalline lattice leads to a solid solution between two end members. If the end members are both metals, the solid solution is referred to as an alloy. In contrast, if two or more metallic elements are mixed in an ordered way on a crystalline lattice, we refer to it as an intermetallic compound.[142] Intermetallic compounds adopt a wide range of crystal structures, ranging from relatively simple structures such as rocksalt and CsCl to highly complex structures and compositions.[143] A prevalent example among nanoscale systems is the disordered alloy vs ordered intermetallic variants of FePt. As-synthesized colloidal nanoparticles of FePt form a fcc alloy with the Fe and Pt atoms randomly distributed among the lattice sites (Figure 12e); these nanoparticles are superparamagnetic. Upon heating, the FePt alloy transforms to an ordered FePt intermetallic, which is ferromagnetic with a high magnetoanisotropy that is desirable for information storage applications.[144] The crystal structure of intermetallic FePt, which adopts the AuCu structure type, is related to that of the fcc alloy of the same composition, but with alternating layers of Fe and Pt and a *c*-axis that is compressed due to this ordering and the differences in the sizes of the Fe and Pt atoms (Figure 12f). A similar thermally induced alloy-to-intermetallic transition occurs for the composition $FePt_3$, with

the intermetallic (adopting the $AuCu_3$ structure type shown in Figure 10l) having Fe localized to the faces of a fcc unit cell and the Pt at the corners.

Several important points about solid solutions are worth noting here. First, in addition to alloys, solid solutions of oxides, chalcogenides, phosphides, and many other classes of materials are also very common. Second, solid solutions are differentiated from the compounds discussed above, where different kinds of atoms sit almost exclusively on different crystallographic sites and therefore are ordered. For example, the composition $LiFeO_2$ can form a disordered solid solution where the Li^+ and Fe^{3+} cations randomly occupy the octahedral cation sites of a rocksalt-type structure (Figure 12g), as well as an ordered compound where the Li^+ and Fe^{3+} reside in alternating layers (Figure 12h).[145,146] Generally, the properties of disordered solid solutions are distinct from the properties of ordered compounds having the same overall composition. Third, solid solutions are typically differentiated from doped materials based on the relative amounts of the elements that are mixed. Dopants are considered to be present in very small amounts, while solid solutions are considered to have more balanced amounts of the elements that are mixed.[147] Finally, complex solid solutions are solid solutions having a large number of end members, where randomization of the constituent elements occurs throughout the crystal structure.[148] Complex solid solutions include high entropy materials, which are considered to have five or more principal elemental components randomly mixed in a crystalline lattice (Figure 12i).[149] Nanoparticles of high entropy materials are rapidly growing in popularity as researchers seek to understand how they form and how unique synergistic properties emerge from interactions among their large number of constituent elements.[150,151]

CRYSTAL STRUCTURES WITH GREATER COMPLEXITY

The preceding sections began with the crystal structures of the metallic elements that are most commonly studied as nanoscale systems and built up to the crystal structures of much more sophisticated compounds with multielement compositions that include both metallic and nonmetallic elements. Throughout these sections, the compositions and crystal structures systematically progressed from simple to more complex. Our descriptions and understanding of the simpler "parent" structures provided a framework for us to describe and understand many of the more complex structures from which they were derived. Complexity, though, is somewhat arbitrary of a term. Some high entropy alloys have more than ten different elements in near-equimolar ratios, and some crystal structures have dozens (or more) of distinct crystallographic sites. It is outside the scope of this Tutorial to cover these more complex crystal structures in depth. However, here we want to highlight a few that are observed among nanoscale systems and that appear to have what could be classified as more complex compositions and/or crystal structures. We choose these examples to emphasize how crystal structures that appear complex at first glance can often be viewed through the framework of simpler components, much like we have done for the other crystal structures presented in this Tutorial. Indeed, typical depictions in the literature for some of these structures make them look intimidating and intractable, but they can be deconstructed into simpler components that are easier to visualize, especially in comparison to the structures we already discussed.

We begin with the sulvanite structure (Figure 13a), which includes compounds such as Cu_3VS_4 and Cu_3NbSe_4 that are of interest for their optical and photocatalytic properties.[152,153] At first glance, one sees a structural framework that is similar to ReO_3 or anti-ReO_3 (Figure 10i,j), with one type of atom at the corners of a cube and another type of atom on each edge halfway between the corner atoms. However, unlike in ReO_3 or anti-ReO_3 which have alternating anions and cations, both types of atoms in these locations are cations, which would (based on electrostatic considerations) not be bonded together. Rather, both cations, which include Cu^+ and V^{5+} in Cu_3VS_4, are bonded to sulfur anions that are in locations mirroring where the cations reside in zincblende or the anions reside in antifluorite. That recognition leads us to look closer at the antifluorite structure (Figure 5f), which also has cations located at all of the same sites that the Cu^+ and V^{5+} cations are located in Cu_3VS_4. Indeed, the sulvanite structure can be described as a cation-ordered variant of antifluorite with half of the cations—those in the center and on the faces—missing. $LaRu_4Sb_{12}$ (Figure 13b), which adopts a so-called filled skutterudite[154] structure, is one of many structurally related compounds of interest for their superconducting and thermoelectric properties. In this structure, one can see the bcc arrangement of the lanthanum atoms, as well as ruthenium atoms that form a smaller cube inside the larger cube formed by the lanthanum atoms at the corners. (The skutterudite structure, typified by $CoSb_3$, is related to filled skutterudite, but without these corner and center atoms where lanthanum is located.) We also find that the ruthenium atoms are each coordinated to six antimony atoms to form a network of cooperatively tilted octahedra. These two instructive examples—sulvanite and filled skutterudite—demonstrate a process by which a structure can be comparatively analyzed and deconstructed into simpler components.

We now turn to tetrahedrite, a mineral containing copper, iron, antimony, and sulfur. We will consider the copper variant without iron, which has a formula of $Cu_{12}Sb_4S_{13}$, since nanostructured $Cu_{12}Sb_4S_{13}$ materials are of interest for their optical and thermoelectric properties.[155,156] This compound complements the sulvanite and filled skutterudite examples by providing an opportunity to deconvolute a complex structure into the polyhedra that comprise it, which helps to simplify it considerably. The $Cu_{12}Sb_4S_{13}$ unit cell is shown in Figure 13c. While there are many (95) atoms included in the unit cell, we can simplify it by focusing on each type of atom individually. We first notice the Sb atoms, which can appear to form a cube similar to that formed by the Ru atoms in $LaRu_4Sb_{12}$ in Figure 13b. However, the Sb atoms in $Cu_{12}Sb_4S_{13}$ are distorted relative to the Ru atoms in $LaRu_4Sb_{12}$. Borrowing from the tools we used to help visualize various characteristics of the rocksalt structure in Figure 3, we show in Figure 13d the structure of $Cu_{12}Sb_4S_{13}$, but with polyhedra instead of the ball-and-stick model. The overlaid polyhedra are challenging to analyze, but if we isolate each type of polyhedron and view it individually, we can get a better sense for how $Cu_{12}Sb_4S_{13}$ is constructed. Figure 13e shows only the octahedra in $Cu_{12}Sb_4S_{13}$, which are formed by central sulfur atoms surrounded by six copper atoms. (Note that the Sb atoms have been removed for clarity.) This view of the tetrahedrite structure simplifies it, showcasing a bcc arrangement of the $S(Cu)_6$ octahedra. Figure 13f shows only the $Cu(S)_4$ tetrahedra, which form from copper sitting at the center of four sulfur atoms. The locations of the tetrahedra may initially seem difficult to analyze, since there are so many of them. However, closer inspection reveals a pattern—each face of the unit cell contains four tetrahedra, with the central copper atoms (highlighted by yellow circles) forming a square that is rotated 45° relative to the x- and y-axes on which the unit cell is oriented. This pattern of tetrahedra gives rise to 24 tetrahedra per unit cell—four interconnected tetrahedra on each of the six faces. The remainder of the polyhedra are trigonal planar arrangements with copper sitting at the center of a triangle formed by sulfur atoms (Figure 13g). Six of these trigonal planar $Cu(S)_3$ units are connected through a central sulfur atom. The result of this configuration is a superoctahedron in the center and on the corners, with each of the six trigonal planar $Cu(S)_3$ units in the center connecting to the square of $Cu(S)_4$ tetrahedra on each of the six faces (Figure 13h).

Pentlandite-type Co_9S_8[157] provides another instructive example of structural deconvolution into polyhedra, but in a system where there is only one type of metal rather than two, as was the case for tetrahedrite. Figure 13i shows the unit cell for Co_9S_8, which includes 107 atoms: 45 cobalt atoms and 62 sulfur atoms. The structure contains a combination of $Co(S)_6$ octahedra and $Co(S)_4$ tetrahedra, which are shown as polyhedra in Figure 13j. For clarity here and in the discussion that follows, we choose different colors for the cobalt atoms in octahedral holes (green) and in tetrahedral holes (yellow). In Figure 13j, we first recognize that the $Co(S)_6$ octahedra are located in the middle of each edge, as well as in the center of the unit cell. Rotating the structure (Figure 13k) and visualizing the polyhedra in this different orientation (Figure 13l) provides greater clarity on where the octahedra and tetrahedra are located relative to one another. Here, we observe that all $Co(S)_6$ octahedra reside in alternating layers, with some tetrahedra among the octahedra in these layers. In the alternating layers that contain no octahedra, $Co(S)_4$ tetrahedra are present, linking together the vertices of the octahedra. Rotating the structure
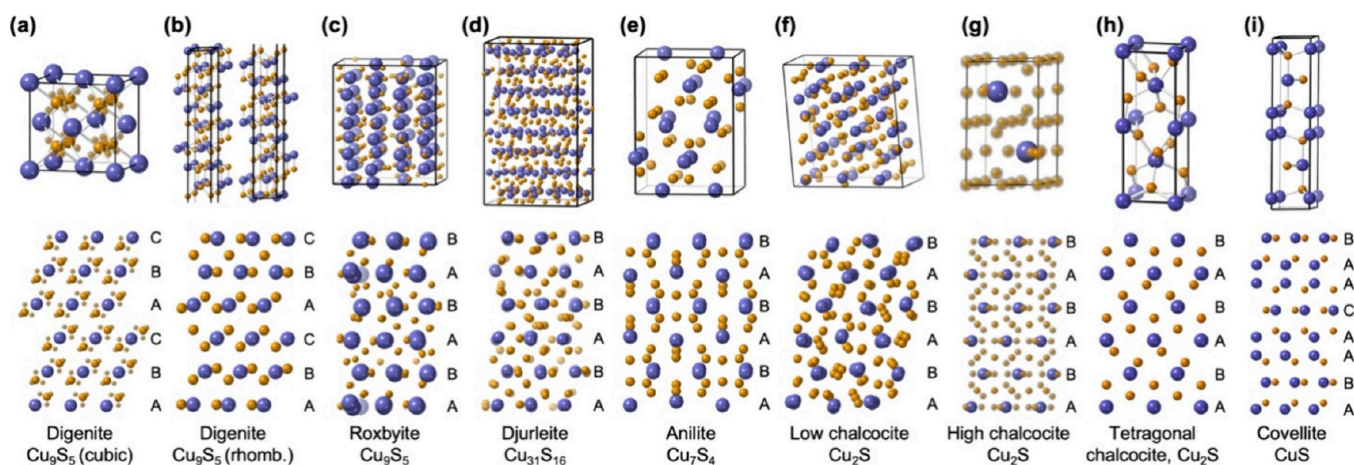
Figure 14. Crystal structures of copper sulfides. Unit cells (top) and corresponding expanded and/or rotated structures (bottom) are shown for nine distinct copper sulfide phases: (a) cubic digenite Cu_9S_5, (b) rhombohedral digenite Cu_9S_5, (c) roxbyite Cu_9S_5, (d) djurleite $Cu_{31}S_{16}$, (e) anilite Cu_7S_4, (f) low chalcocite Cu_2S, (g) high chalcocite Cu_2S, (h) tetragonal chalcocite Cu_2S, and (i) covellite CuS. The unit cells look quite different from one another, but the rotated and expanded structures allow almost all of them to be related to a ABCABC or ABAB close-packed sulfur structure, as indicated, with or without distortions. For cubic digenite and high chalcocite, the blurred copper atoms indicate partial occupancy and therefore disorder over the multiple crystallographic sites indicated. For rhombohedral digenite, the unit cell has a high aspect ratio and is therefore split over two columns; the four copper atoms on the bottom of the top half of the cell (to the left) are the same copper atoms as shown on the top of the bottom half of the cell (to the right).

again (Figure 13m) places it in an orientation that reveals the familiar ABCABC stacking sequence of ccp sulfur layers. Integrating the polyhedra in this orientation (Figure 13n) shows a different view of how the octahedra are separated from one another by the tetrahedra. Close inspection of this orientation also reveals an important feature of this structure that contributes significantly to the properties of Co_9S_8, while also placing limitations on the types of compounds that can adopt this structure. Several of the $Co(S)_4$ tetrahedra in the Co_9S_8 structure connect with each other through their edges instead of their corners (Figure 13n). This arrangement places the metal atoms in the tetrahedral holes within close contact, leading to metallic conductivity and making this structure viable only for metals capable of metal–metal interactions, as is the case for cobalt.

Given their longstanding use as hydrodesulfurization catalysts and their more recently discovered use as catalysts for the hydrogen evolution reaction, nanoparticles of transition metal phosphides have been widely studied across the energy sciences.[158,159] As an additional example, we showcase CoP.[160] The transition metal phosphides[161] form compounds that span a wide range of compositions, including various empirical formulas for the same metal. Using the Ni–P system as an example, synthetically accessible phosphides include the metal-rich phosphides Ni_3P, $Ni_{12}P_5$, Ni_2P, and Ni_5P_4, as well as NiP, NiP_2, and NiP_3 which are referred to as polyphosphides[162] because of their P–P bonds. Many of these crystal structures can initially appear somewhat complex. Returning to CoP, the unit cell, shown in Figure 13o, looks unremarkable—four cobalt atoms and four phosphorus atoms. Upon expanding and rotating the structure (a common process we've now used several times for helping to visualize features), we make an interesting observation. In this orientation, we see the familiar ABAB stacking sequence of phosphorus layers that we recognize from hcp structures. CoP is not a close-packed structure, but much like the TMDs, we can still use the ABAB formalism to understand how the structure is derived. Here, one-dimensional zigzag chains of phosphorus atoms line up in parallel to form

planes. Within each plane, alternating zigzag chains of phosphorus atoms are in opposite orientations with respect to each other—up/down/up/down vs down/up/down/up. These planes, which are much more complex than simple close-packed planes, then stack vertically in an ABAB arrangement, with cobalt atoms sitting in highly distorted octahedral sites.

The examples in Figure 13 provide insights into how crystal structures that initially appear to be complex can sometimes be deconstructed into components that are much simpler, which helps us to understand how they are derived and how they are related to one another. Figure 14 provides one final example. Here, we focus on the copper sulfides, which are notorious for the wide range of different compositions that form, the ability for the same composition to adopt different crystal structures, and the complicated nature of their crystal structures. Figure 14a-i shows, along the top row, the unit cells for nine different copper sulfides. Most of these copper sulfides are routinely synthesized[163] and used as nanoparticles because of their tunable plasmonic and catalytic properties,[164] as well as for their use as templates in topochemical cation exchange-based transformation to other compositions.[165,166] Initial inspection of the unit cells, which span a range of sizes and symmetries, suggests that they all are very different from one another. Digenite (Figure 14a) is cubic and high chalcocite (Figure 14g) is hexagonal; both have copper cations that are disordered over several crystallographic sites. Rhombohedral digenite (Figure 14b) has such a tall unit cell that we had to divide it in half to show it in the allotted space. Low chalcocite (Figure 14f), roxbyite (Figure 14c), and djurleite (Figure 14d) have 144, 180, and 376 atoms in their unit cells, respectively. Tetragonal chalcocite (Figure 14h) and covellite (Figure 14i) have unit cells with high aspect ratios (but not nearly as high of an aspect ratio as rhombohedral digenite).[167] How do we make sense of all of this?

The bottom row in Figure 14 applies what we have been doing throughout this Tutorial—increasing (or decreasing) the number of unit cells being viewed and rotating in different ways to see what other features can become visible as we look at the crystal structures in different orientations. Despite the

dramatically different unit cell presentations for the nine different copper sulfides in Figure 14, all of them can be analyzed through the lens of either ccp-like or hcp-like structures. Cubic digenite (Figure 14a) is closely related to the antifluorite structure, with a ABCABC array of sulfide anions with tetrahedral holes filled by copper cations. Cubic digenite is nonstoichiometric relative to antifluorite (i.e., $Cu_{1.8}S$ instead of Cu_2S), and therefore has cation vacancies. (The blurred atoms in the structure shown in Figure 14a represent crystallographic sites on which cations are disordered and distributed, and from which vacancies emerge.) Rhombohedral digenite (Figure 14b) has a similar ABCABC array of sulfide anions with copper cations occupying tetrahedral holes. The unit cell for rhombohedral digenite is quite tall, as is needed to capture a large superlattice that arises from the long-range ordering of the copper cations. The structure of roxbyite (Figure 14c), which also has a formula of $Cu_{1.8}S$, can be approximated by a hcp-like arrangement of sulfur anions. These hcp-like sulfur layers are significantly distorted, but their ABAB stacking sequence is clearly observable. The copper cations sit in a variety of low-coordinate sites. Djurleite (Figure 14d) is similar to roxbyite, also having a distorted hcp-like sulfur structure with copper cations occupying several types of crystallographic sites. Djurleite, which has a formula of $Cu_{1.93}S$, is slightly more copper-rich than roxbyite and digenite. Anilite (Figure 14e) and low chalcocite (Figure 14f) also have distorted hcp-like sulfur structures with copper cations sitting in various crystallographic sites; anilite is copper-deficient ($Cu_{1.75}S$) while low chalcocite is stoichiometric (Cu_2S). High chalcocite, also Cu_2S, returns to a nondistorted ABAB sulfur structure (Figure 14g), but with copper cations that are disordered across a large number of different crystallographic sites, each of which are only partially occupied. Tetragonal chalcocite (Figure 14h) is not considered to have a close-packed anion structure, but rather a sulfur arrangement that is more in line with a body centered tetragonal structure. However, the structure of tetragonal chalcocite is closely related to that of digenite; describing this relationship is beyond the scope of this Tutorial, but has been detailed elsewhere.[168] Finally, covellite (Figure 14i) can be viewed as having a nominal AABAAC stacking sequence of sulfur layers. The "B" and "C" layers have 3-coordinate copper atoms at the center of a triangle of sulfur atoms, while in the A layers tetrahedrally coordinated copper atoms sit above or below the sulfur atoms.

CRYSTAL STRUCTURES IN NANOPARTICLE ASSEMBLY

The crystal structures that we discussed in this Tutorial show up in many places in nanoscale materials systems. Some of the most prominent examples occur when nanoparticles, or mixtures of nanoparticles, are assembled into superlattices.[169] In such cases, nanoparticles are considered as "artificial atoms", as nanoparticles having uniform sizes can pack together in much the same way that atoms pack together to form crystals. Uniform spherical nanoparticles best approximate the spherical shapes of atoms, and it is therefore not surprising that monodisperse populations of nanoparticles frequently assemble into close-packed structures. Figure 15a shows a transmission electron microscopy (TEM) image of a close-packed bilayer of 12.8 nm spherical Fe_3O_4 nanoparticles;[170] the "A" and "B" layers, noted in Figures 3a and 3b, are visible in the TEM image. Binary mixtures of two distinct populations of uniform nanoparticles having different sizes can cocrystallize into common ionic crystal
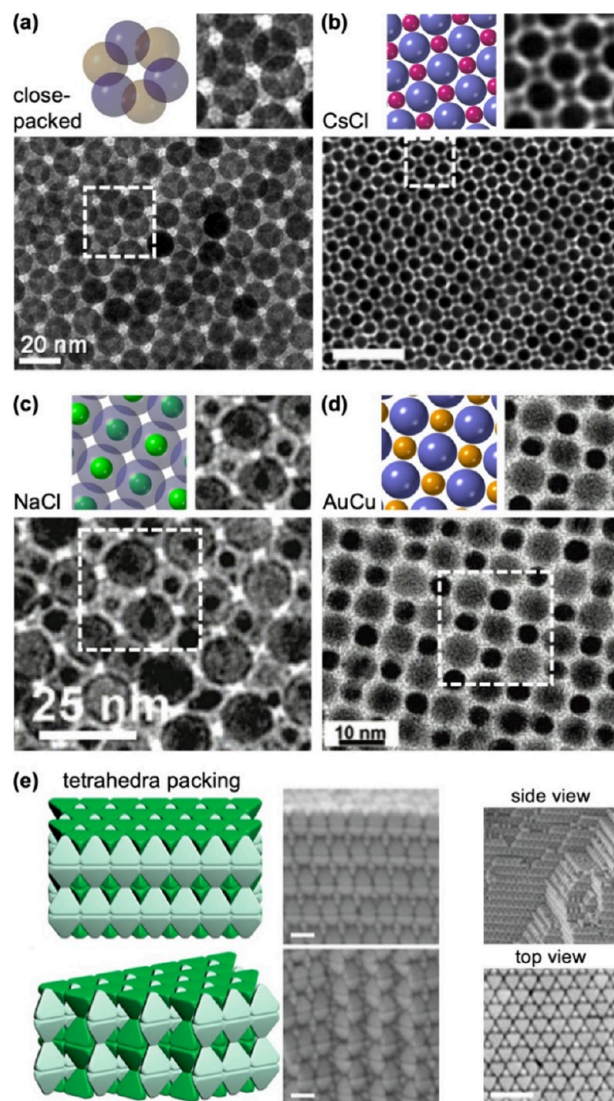

Figure 15. Nanoparticle superlattices that form different crystal structures. TEM images of (a) a close-packed bilayer of 12.8 nm Fe_3O_4 nanoparticles,[170] (b) a CsCl-structured superlattice formed from the coassembly of 5.4 nm Ag and 9.3 nm PbS nanoparticles,[171] (c) a NaCl-structured superlattice formed from the coassembly of 13.4 nm Fe_2O_3 and 5.0 nm Au nanoparticles,[172] and (d) a AuCu-structured superlattice formed from the coassembly of 7.6 nm PbSe and 5.0 nm Au nanoparticles.[172] For each panel, full TEM images are shown at the bottom, while the enlarged region indicated by the white dashed box is shown at the top, along with a representation of the corresponding crystal structure in the same orientation. (e) TEM images of superlattices formed from the assembly of tetrahedron-shaped gold nanoparticles, along with corresponding diagrams to show the nature of the packing.[173] Panel (a) is adapted with permission from ref 170, copyright 2012 American Chemical Society. Panel (b) is adapted with permission from ref 170, copyright 2013 American Chemical Society. Panels (c) and (d) are adapted with permission from ref 172, copyright 2006 American Chemical Society. Panel (e) is adapted with permission from ref 173, copyright 2022 American Chemical Society.

structures. For example, Figure 15b shows a TEM image of a CsCl-structured binary superlattice formed from the coassembly of spherical 5.4 nm Ag and 9.3 nm PbS nanoparticles.[171] A TEM image of a NaCl-structured binary nanoparticle superlattice, formed from spherical 13.4 nm Fe_2O_3 and 5.0 nm Au nanoparticles, is shown Figure 15c, while Figure 15d shows a

AuCu-structured assembly formed from spherical 7.6 nm PbSe and 5.0 nm Au nanoparticles.[172] These are just some of the many structures that are encountered in assembled nanoparticle systems. Nanoparticles having shapes that mimic the various coordination polyhedra we discussed can also assemble into superlattices that resemble the various ways in which polyhedra connect to one another within crystal structures. For example, Figure 15e shows a type of superlattice encountered from the assembly and crystallization of tetrahedron-shaped gold nanoparticles.[173] Here, the tetrahedra share faces, and these face-sharing tetrahedral units interdigitate to form the long-range ordered structure.

CONCLUSIONS AND PERSPECTIVES

In this Tutorial, we highlighted key aspects of how various types of crystal structures are described, visualized, related, and derived. We progressed from simple to more complex, in terms of both composition and crystal structure. In doing so, we highlighted how many of the foundational structural components of simple crystal structures manifest in seemingly more complex structures. These structural features can often be viewed as building blocks that stack, connect, and interleave in various ways to derive different structures that at first glance may appear to be quite different, but in reality, may be closely related. This formalism, which is already well established in solid-state chemistry, is important to recognize and apply within nanoscale systems as well, given the diverse ways in which crystal structures play a fundamental role in the synthesis, properties, and applications of nanoscale materials and assemblies. Additionally, rapidly accelerating capabilities in the computational prediction of new crystal structures (and new structures for a given composition) are providing increasingly fertile ground for the development and discovery of new nanoscale materials, for which details of crystal structures may provide the primary novelty. Materials Project,[23] an online database that currently contains computed crystal structures of more than 150,000 different compounds, is one example of a resource that provides almost countless opportunities for visualizing, comparing, and rationalizing crystal structures—many that are experimentally observed but many that have only been predicted. As has been the case in the past, transformative future advances in nanoscience and nanotechnology are likely to come from new phenomena and capabilities that arise from the expanded study and application of compounds, concepts, and tools from solid-state chemistry.

This Tutorial focused on the long-range crystalline structures of inorganic materials, which from a nanoscience perspective, may be considered as describing the "bulk" of a nanocrystal. However, it is important to recognize that in nanocrystals, the local structure, including coordination geometries and distortions, may differ from that which is expected for the long-range bulk structure due to the effects of surface energies and other size-dependent phenomena. Characterization that considers local structure and bonding, such as pair distribution function (PDF) analysis, X-ray absorption spectroscopy (XAS), and nuclear magnetic resonance (NMR) spectroscopy, is also important for identifying and understanding potential differences in bulk versus nanoscale materials, including both their structures and their properties.

ASSOCIATED CONTENT

Supporting Information

The Supporting Information is available free of charge at https://pubs.acs.org/doi/10.1021/acsnanoscienceau.4c00010.

Selected crystal structure files in both CrystalMaker (.cdmf) and crystallographic information file (.cif) formats, along with an explanatory text file (ZIP)

Selected crystal structures with superimposed crystallographic axes (PDF)

AUTHOR INFORMATION

Corresponding Author

Raymond E. Schaak — *Department of Chemistry, Department of Chemical Engineering, and Materials Research Institute, The Pennsylvania State University, University Park, Pennsylvania 16802, United States;* orcid.org/0000-0002-7468-8181; Email: res20@psu.edu

Author

Katelyn J. Baumler — *Department of Chemistry, The Pennsylvania State University, University Park, Pennsylvania 16802, United States;* orcid.org/0000-0001-7386-836X

Complete contact information is available at:
https://pubs.acs.org/10.1021/acsnanoscienceau.4c00010

Notes

The authors declare no competing financial interest.

REFERENCES

(1) Hoffmann, R. How Chemistry and Physics Meet in the Solid State. *Angew. Chem., Int. Ed. Engl.* **1987**, 26, 846−878.

(2) Xia, Y.; Xiong, Y.; Lim, B.; Skrabalak, S. E. Shape-Controlled Synthesis of Metal Nanocrystals: Simple Chemistry Meets Complex Physics? *Angew. Chem., Int. Ed.* **2009**, 48, 60−103.

(3) Roldan Cuenya, B. Metal Nanoparticle Catalysts Beginning to Shape-Up. *Acc. Chem. Res.* **2013**, 46, 1682−1691.

(4) De Gregorio, G. L.; Burdyny, T.; Loiudice, A.; Iyengar, P.; Smith, W. A.; Buonsanti, R. Facet-Dependent Selectivity of Cu Catalysts in Electrochemical CO_2 Reduction at Commercially Viable Current Densities. *ACS Catal.* **2020**, 10, 4854−4862.

(5) Zhang, Q.; Wang, H. Facet-Dependent Catalytic Activities of Au Nanoparticles Enclosed by High-Index Facets. *ACS Catal.* **2014**, 4, 4027−4033.

(6) Buck, M. R.; Schaak, R. E. Emerging Strategies for the Total Synthesis of Inorganic Nanostructures. *Angew. Chem., Int. Ed.* **2013**, 52, 6154−6178.

(7) Xia, Y.; Gilroy, K. D.; Peng, H.-C.; Xia, X. Seed-Mediated Growth of Colloidal Metal Nanocrystals. *Angew. Chem., Int. Ed.* **2017**, 56, 60−95.

(8) Marbella, L. E.; Chevrier, D. M.; Tancini, P. D.; Shobayo, O.; Smith, A. M.; Johnston, K. A.; Andolina, C. M.; Zhang, P.; Mpourmpakis, G.; Millstone, J. E. Description and Role of Bimetallic

Prenucleation Species in the Formation of Small Nanoparticle Alloys. *J. Am. Chem. Soc.* **2015**, *137*, 15852−15858.

(9) Wikibooks contributors. *Introduction to Inorganic Chemistry*; Wikibooks. https://en.wikibooks.org/wiki/Introduction_to_Inorganic_Chemistry.

(10) Smart, L. E.; Moore, E. A. *Solid State Chemistry: An Introduction*, Fourth ed.; CRC Press, 2012.

(11) West, A. R. *Solid State Chemistry and Its Applications*; John Wiley & Sons, 1991.

(12) Woodward, P. M.; Karen, P.; Evans, J. S. O.; Vogt, T. *Solid State Materials Chemistry*; Cambridge University Press, 2021.

(13) Rao, C. N. R.; Gopalakrishnan, J. *New Directions in Solid State Chemistry*; Cambridge University Press, 1997.

(14) Douglas, B.; Ho, S.-M. *Structure and Chemistry of Crystalline Solids*; Springer Science & Business Media, 2007.

(15) Müller, U. *Inorganic Structural Chemistry*; Wiley, 2007.

(16) Steurer, W. 1 - Crystal Structures of Metallic Elements and Compounds. In *Physical Metallurgy*, Fifth ed.; Laughlin, D. E., Hono, K., Eds.; Elsevier: Oxford, 2014; pp 1−101. DOI: 10.1016/B978-0-444-53770-6.00001-0.

(17) Douglas, B. E. Stuffed Derivatives of Close-Packed Structures. *J. Chem. Educ.* **2007**, *84*, 1846.

(18) Trolier-McKinstry, S.; Newnham, R. E. *Materials Engineering: Bonding, Structure, and Structure-Property Relationships*; Cambridge University Press, 2018.

(19) Holder, C. F.; Schaak, R. E. Tutorial on Powder X-Ray Diffraction for Characterizing Nanoscale Materials. *ACS Nano* **2019**, *13*, 7359−7365.

(20) Rao, C. N. R.; Biswas, K. Characterization of Nanomaterials by Physical Methods. *Annu. Rev. Anal. Chem.* **2009**, *2*, 435−462.

(21) *CrystalMaker: A Crystal and Molecular Structures Program for Mac and Windows*. www.crystalmaker.com (accessed 2024−05−07).

(22) Villars, P. *Pearson's Handbook Desk ed. Crystallographic Data for Intermetallic Phases*; ASM International: Materials Park, OH.

(23) Jain, A.; Ong, S. P.; Hautier, G.; Chen, W.; Richards, W. D.; Dacek, S.; Cholia, S.; Gunter, D.; Skinner, D.; Ceder, G.; Persson, K. A. Commentary: The Materials Project: A Materials Genome Approach to Accelerating Materials Innovation. *APL Mater.* **2013**, *1*, 011002.

(24) Hang, Y.; Wang, A.; Wu, N. Plasmonic Silver and Gold Nanoparticles: Shape- and Structure-Modulated Plasmonic Functionality for Point-of-Caring Sensing, Bio-Imaging and Medical Therapy. *Chem. Soc. Rev.* **2024**, *53*, 2932−2971.

(25) Xie, C.; Niu, Z.; Kim, D.; Li, M.; Yang, P. Surface and Interface Control in Nanoparticle Catalysis. *Chem. Rev.* **2020**, *120*, 1184−1249.

(26) Shi, Y.; Lyu, Z.; Zhao, M.; Chen, R.; Nguyen, Q. N.; Xia, Y. Noble-Metal Nanocrystals with Controlled Shapes for Catalytic and Electrocatalytic Applications. *Chem. Rev.* **2021**, *121*, 649−735.

(27) Bentley, A. K.; Skrabalak, S. E. A Primer on Lattice Planes, Crystal Facets, and Nanoparticle Shape Control. *J. Chem. Educ.* **2023**, *100*, 3425−3433.

(28) Quan, Z.; Wang, Y.; Fang, J. High-Index Faceted Noble Metal Nanocrystals. *Acc. Chem. Res.* **2013**, *46*, 191−202.

(29) Oh, S. J.; Berry, N. E.; Choi, J.-H.; Gaulding, E. A.; Lin, H.; Paik, T.; Diroll, B. T.; Muramoto, S.; Murray, C. B.; Kagan, C. R. Designing High-Performance PbS and PbSe Nanocrystal Electronic Devices through Stepwise, Post-Synthesis, Colloidal Atomic Layer Deposition. *Nano Lett.* **2014**, *14*, 1559−1566.

(30) Joo, J.; Na, H. B.; Yu, T.; Yu, J. H.; Kim, Y. W.; Wu, F.; Zhang, J. Z.; Hyeon, T. Generalized and Facile Synthesis of Semiconducting Metal Sulfide Nanocrystals. *J. Am. Chem. Soc.* **2003**, *125*, 11100−11105.

(31) Brewster, D. A.; Bian, Y.; Knowles, K. E. Direct Solvothermal Synthesis of Phase-Pure Colloidal NiO Nanocrystals. *Chem. Mater.* **2020**, *32*, 2004−2013.

(32) Guler, U.; Suslov, S.; Kildishev, A. V.; Boltasseva, A.; Shalaev, V. M. Colloidal Plasmonic Titanium Nitride Nanoparticles: Properties and Applications. *Nanophotonics* **2015**, *4*, 269−276.

(33) Antunez, P. D.; Buckley, J. J.; Brutchey, R. L. Tin and Germanium Monochalcogenide IV−VI Semiconductor Nanocrystals for Use in Solar Cells. *Nanoscale* **2011**, *3*, 2399−2411.

(34) Kobayashi, A.; Suzuki, Y.; Ohba, T.; Noro, S.; Chang, H.-C.; Kato, M. Ln−Co-Based Rock-Salt-Type Porous Coordination Polymers: Vapor Response Controlled by Changing the Lanthanide Ion. *Inorg. Chem.* **2011**, *50*, 2061−2063.

(35) Leonard, B. M.; Schaak, R. E. Multistep Solution-Mediated Formation of AuCuSn₂: Mechanistic Insights for the Guided Design of Intermetallic Solid-State Materials and Complex Multimetal Nanocrystals. *J. Am. Chem. Soc.* **2006**, *128*, 11475−11482.

(36) Schneider, J.; Matsuoka, M.; Takeuchi, M.; Zhang, J.; Horiuchi, Y.; Anpo, M.; Bahnemann, D. W. Understanding TiO_2 Photocatalysis: Mechanisms and Materials. *Chem. Rev.* **2014**, *114*, 9919−9986.

(37) Shi, Q.; Zhu, C.; Du, D.; Lin, Y. Robust Noble Metal-Based Electrocatalysts for Oxygen Evolution Reaction. *Chem. Soc. Rev.* **2019**, *48*, 3181−3192.

(38) Tavares, S.; Yang, K.; Meyers, M. A. Heusler Alloys: Past, Properties, New Alloys, and Prospects. *Prog. Mater. Sci.* **2023**, *132*, 101017.

(39) Trovarelli, A.; Llorca, J. Ceria Catalysts at Nanoscale: How Do Crystal Shapes Shape Catalysis? *ACS Catal.* **2017**, *7*, 4716−4735.

(40) Kumari, N.; Sareen, S.; Verma, M.; Sharma, S.; Sharma, A.; Sohal, H. S.; Mehta, S. K.; Park, J.; Mutreja, V. Zirconia-Based Nanomaterials: Recent Developments in Synthesis and Applications. *Nanoscale Adv.* **2022**, *4*, 4210−4236.

(41) Ye, X.; Collins, J. E.; Kang, Y.; Chen, J.; Chen, D. T. N.; Yodh, A. G.; Murray, C. B. Morphologically Controlled Synthesis of Colloidal Upconversion Nanophosphors and Their Shape-Directed Self-Assembly. *Proc. Natl. Acad. Sci. U.S.A.* **2010**, *107*, 22430−22435.

(42) Butterfield, A. G.; Alameda, L. T.; Schaak, R. E. Emergence and Control of Stacking Fault Formation during Nanoparticle Cation Exchange Reactions. *J. Am. Chem. Soc.* **2021**, *143*, 1779−1783.

(43) Fenton, J. L.; Steimle, B. C.; Schaak, R. E. Structure-Selective Synthesis of Wurtzite and Zincblende ZnS, CdS, and $CuInS_2$ Using Nanoparticle Cation Exchange Reactions. *Inorg. Chem.* **2019**, *58*, 672−678.

(44) Rogach, A. *Semiconductor Nanocrystal Quantum Dots: Synthesis, Assembly, Spectroscopy and Applications*; Springer, 2008.

(45) Trindade, T.; O'Brien, P.; Pickett, N. L. Nanocrystalline Semiconductors: Synthesis, Properties, and Perspectives. *Chem. Mater.* **2001**, *13*, 3843−3858.

(46) El-Sayed, M. A. Small Is Different: Shape-, Size-, and Composition-Dependent Properties of Some Colloidal Semiconductor Nanocrystals. *Acc. Chem. Res.* **2004**, *37*, 326−333.

(47) Smith, A. M.; Nie, S. Semiconductor Nanocrystals: Structure, Properties, and Band Gap Engineering. *Acc. Chem. Res.* **2010**, *43*, 190−200.

(48) Coughlan, C.; Ibáñez, M.; Dobrozhan, O.; Singh, A.; Cabot, A.; Ryan, K. M. Compound Copper Chalcogenide Nanocrystals. *Chem. Rev.* **2017**, *117*, 5865−6109.

(49) Lei, Y.; Zhang, T.; Lin, Y.-C.; Granzier-Nakajima, T.; Bepete, G.; Kowalczyk, D. A.; Lin, Z.; Zhou, D.; Schranghamer, T. F.; Dodda, A.; Sebastian, A.; Chen, Y.; Liu, Y.; Pourtois, G.; Kempa, T. J.; Schuler, B.; Edmonds, M. T.; Quek, S. Y.; Wurstbauer, U.; Wu, S. M.; Glavin, N. R.; Das, S.; Dash, S. P.; Redwing, J. M.; Robinson, J. A.; Terrones, M. Graphene and Beyond: Recent Advances in Two-Dimensional Materials Synthesis, Properties, and Devices. *ACS Nanosci. Au* **2022**, *2*, 450−485.

(50) Sun, Y.; Terrones, M.; Schaak, R. E. Colloidal Nanostructures of Transition-Metal Dichalcogenides. *Acc. Chem. Res.* **2021**, *54*, 1517−1527.

(51) Das, S.; Robinson, J. A.; Dubey, M.; Terrones, H.; Terrones, M. Beyond Graphene: Progress in Novel Two-Dimensional Materials and van Der Waals Solids. *Annu. Rev. Mater. Res.* **2015**, *45*, 1−27.

(52) Butler, S. Z.; Hollen, S. M.; Cao, L.; Cui, Y.; Gupta, J. A.; Gutiérrez, H. R.; Heinz, T. F.; Hong, S. S.; Huang, J.; Ismach, A. F.; Johnston-Halperin, E.; Kuno, M.; Plashnitsa, V. V.; Robinson, R. D.; Ruoff, R. S.; Salahuddin, S.; Shan, J.; Shi, L.; Spencer, M. G.; Terrones, M.; Windl, W.; Goldberger, J. E. Progress, Challenges, and Opportunities in Two-Dimensional Materials Beyond Graphene. *ACS Nano* **2013**, *7*, 2898−2926.

(53) Schaak, R. E.; Klimczuk, T.; Foo, M. L.; Cava, R. J. Superconductivity Phase Diagram of $Na_xCoO_2 \cdot 1.3H_2O$. *Nature* **2003**, *424*, 527−529.

(54) Lee, M.; Viciu, L.; Li, L.; Wang, Y.; Foo, M. L.; Watauchi, S.; Pascal, R. A., Jr; Cava, R. J.; Ong, N. P. Large Enhancement of the Thermopower in Na_xCoO_2 at High Na Doping. *Nat. Mater.* **2006**, *5*, 537−540.

(55) Rai, A. K.; Anh, L. T.; Gim, J.; Mathew, V.; Kim, J. Electrochemical Properties of Na_xCoO_2 ($x \sim 0.71$) Cathode for Rechargeable Sodium-Ion Batteries. *Ceram. Int.* **2014**, *40*, 2411−2417.

(56) Bux, S. K.; Fleurial, J.-P.; Kaner, R. B. Nanostructured Materials for Thermoelectric Applications. *Chem. Commun.* **2010**, *46*, 8311−8324.

(57) Liu, P.; Williams, J. R.; Cha, J. J. Topological Nanomaterials. *Nat. Rev. Mater.* **2019**, *4*, 479−496.

(58) Ma, F.; Zhou, M.; Jiao, Y.; Gao, G.; Gu, Y.; Bilic, A.; Chen, Z.; Du, A. Single Layer Bismuth Iodide: Computational Exploration of Structural, Electrical, Mechanical and Optical Properties. *Sci. Rep.* **2015**, *5*, 17558.

(59) Xia, J.; Yan, J.; Shen, Z. X. Transition Metal Dichalcogenides: Structural, Optical and Electronic Property Tuning via Thickness and Stacking. *FlatChem* **2017**, *4*, 1−19.

(60) Sokolikova, M. S.; Mattevi, C. Direct Synthesis of Metastable Phases of 2D Transition Metal Dichalcogenides. *Chem. Soc. Rev.* **2020**, *49*, 3952−3980.

(61) Allen, M. J.; Tung, V. C.; Kaner, R. B. Honeycomb Carbon: A Review of Graphene. *Chem. Rev.* **2010**, *110*, 132−145.

(62) Bianco, E.; Butler, S.; Jiang, S.; Restrepo, O. D.; Windl, W.; Goldberger, J. E. Stability and Exfoliation of Germanane: A Germanium Graphane Analogue. *ACS Nano* **2013**, *7*, 4414−4421.

(63) Liu, H.; Neal, A. T.; Zhu, Z.; Luo, Z.; Xu, X.; Tománek, D.; Ye, P. D. Phosphorene: An Unexplored 2D Semiconductor with a High Hole Mobility. *ACS Nano* **2014**, *8*, 4033−4041.

(64) Mannix, A. J.; Zhou, X.-F.; Kiraly, B.; Wood, J. D.; Alducin, D.; Myers, B. D.; Liu, X.; Fisher, B. L.; Santiago, U.; Guest, J. R.; Yacaman, M. J.; Ponce, A.; Oganov, A. R.; Hersam, M. C.; Guisinger, N. P. Synthesis of Borophenes: Anisotropic, Two-Dimensional Boron Polymorphs. *Science* **2015**, *350*, 1513−1516.

(65) Anasori, B.; Lukatskaya, M. R.; Gogotsi, Y. 2D Metal Carbides and Nitrides (MXenes) for Energy Storage. *Nat. Rev. Mater.* **2017**, *2*, 1−17.

(66) Alameda, L. T.; Moradifar, P.; Metzger, Z. P.; Alem, N.; Schaak, R. E. Topochemical Deintercalation of Al from MoAlB: Stepwise Etching Pathway, Layered Intergrowth Structures, and Two-Dimensional MBene. *J. Am. Chem. Soc.* **2018**, *140*, 8833−8840.

(67) Zhou, J.; Palisaitis, J.; Halim, J.; Dahlqvist, M.; Tao, Q.; Persson, I.; Hultman, L.; Persson, P. O. Å.; Rosen, J. Boridene: Two-Dimensional $Mo_{4/3}B_{2-x}$ with Ordered Metal Vacancies Obtained by Chemical Exfoliation. *Science* **2021**, *373*, 801−805.

(68) Alameda, L. T.; Baumler, K. J.; Katzbaer, R. R.; Schaak, R. E. Soft Chemistry of Hard Materials: Low-Temperature Pathways to Bulk and Nanostructured Layered Metal Borides. *Acc. Chem. Res.* **2023**, *56*, 3515−3524.

(69) Schaak, R. E.; Mallouk, T. E. Perovskites by Design: A Toolbox of Solid-State Reactions. *Chem. Mater.* **2002**, *14*, 1455−1471.

(70) Xiao, X.; Wang, H.; Urbankowski, P.; Gogotsi, Y. Topochemical Synthesis of 2D Materials. *Chem. Soc. Rev.* **2018**, *47*, 8744−8765.

(71) Uppuluri, R.; Sen Gupta, A.; Rosas, A. S.; Mallouk, T. E. Soft Chemistry of Ion-Exchangeable Layered Metal Oxides. *Chem. Soc. Rev.* **2018**, *47*, 2401−2430.

(72) Lim, K. R. G.; Shekhirev, M.; Wyatt, B. C.; Anasori, B.; Gogotsi, Y.; Seh, Z. W. Fundamentals of MXene Synthesis. *Nat. Synth.* **2022**, *1*, 601−614.

(73) Alameda, L. T.; Lord, R. W.; Barr, J. A.; Moradifar, P.; Metzger, Z. P.; Steimle, B. C.; Holder, C. F.; Alem, N.; Sinnott, S. B.; Schaak, R. E. Multi-Step Topochemical Pathway to Metastable Mo_2AlB_2 and Related Two-Dimensional Nanosheet Heterostructures. *J. Am. Chem. Soc.* **2019**, *141*, 10852−10861.

(74) Baumler, K. J.; Adams, O. S.; Schaak, R. E. One-Step Topochemical Transformation of MoAlB into Metastable Mo_2AlB_2 Using a Metal Chloride Salt Reaction. *Chem. Commun.* **2023**, *59*, 4814−4817.

(75) Andersen, H. L.; Saura-Muzquiz, M.; Granados-Miralles, C.; Canevet, E.; Lock, N.; Christensen, M. Crystalline and Magnetic Structure−Property Relationship in Spinel Ferrite Nanoparticles. *Nanoscale* **2018**, *10*, 14902−14914.

(76) Zhao, Q.; Yan, Z.; Chen, C.; Chen, J. Spinels: Controlled Preparation, Oxygen Reduction/Evolution Reaction Application, and Beyond. *Chem. Rev.* **2017**, *117*, 10121−10211.

(77) Li, C.; Han, X.; Cheng, F.; Hu, Y.; Chen, C.; Chen, J. Phase and Composition Controllable Synthesis of Cobalt Manganese Spinel Nanoparticles towards Efficient Oxygen Electrocatalysis. *Nat. Commun.* **2015**, *6*, 7345.

(78) Diodati, S.; Walton, R. I.; Mascotto, S.; Gross, S. Low-Temperature Wet Chemistry Synthetic Approaches towards Ferrites. *Inorg. Chem. Front.* **2020**, *7*, 3282−3314.

(79) Li, H.; Yang, S.; Hui, D.; Hong, R. Progress in Magnetic Fe_3O_4 Nanomaterials in Magnetic Resonance Imaging. *Nanotechnol. Rev.* **2020**, *9*, 1265−1283.

(80) Zhou, H.; Mayorga-Martinez, C. C.; Pané, S.; Zhang, L.; Pumera, M. Magnetically Driven Micro and Nanorobots. *Chem. Rev.* **2021**, *121*, 4999−5041.

(81) Roldan, A.; Hollingsworth, N.; Roffey, A.; Islam, H.-U.; Goodall, J. B. M.; Catlow, C. R. A.; Darr, J. A.; Bras, W.; Sankar, G.; Holt, K. B.; Hogarth, G.; de Leeuw, N. H. Bio-Inspired CO_2 Conversion by Iron Sulfide Catalysts under Sustainable Conditions. *Chem. Commun.* **2015**, *51*, 7501−7504.

(82) Choi, J.-H.; Wang, H.; Oh, S. J.; Paik, T.; Sung, P.; Sung, J.; Ye, X.; Zhao, T.; Diroll, B. T.; Murray, C. B.; Kagan, C. R. Exploiting the Colloidal Nanocrystal Library to Construct Electronic Devices. *Science* **2016**, *352*, 205−208.

(83) Tamirat, A. G.; Rick, J.; Dubale, A. A.; Su, W.-N.; Hwang, B.-J. Using Hematite for Photoelectrochemical Water Splitting: A Review of Current Progress and Challenges. *Nanoscale Horiz.* **2016**, *1*, 243−267.

(84) Robinson, P.; Harrison, R. J.; McEnroe, S. A.; Hargraves, R. B. Lamellar Magnetism in the Haematite−Ilmenite Series as an Explanation for Strong Remanent Magnetization. *Nature* **2002**, *418*, 517−520.

(85) Guo, S.; Huang, R.; Yuan, J.; Chen, R.; Chen, F. Efficient Removal of Aromatic Pollutants via Catalytic Wet Peroxide Oxidation over Synthetic Anisotropic Ilmenite/Carbon Nanocomposites. *npj Clean Water* **2023**, *6*, 1−12.

(86) Bhalla, A. S.; Guo, R.; Roy, R. The Perovskite Structure—a Review of Its Role in Ceramic Science and Technology. *Mater. Res. Innov.* **2000**, *4*, 3−26.

(87) Peña, M. A.; Fierro, J. L. G. Chemical Structures and Performance of Perovskite Oxides. *Chem. Rev.* **2001**, *101*, 1981−2018.

(88) Fu, Y.; Zhu, H.; Chen, J.; Hautzinger, M. P.; Zhu, X.-Y.; Jin, S. Metal Halide Perovskite Nanostructures for Optoelectronic Applications and the Study of Physical Properties. *Nat. Rev. Mater.* **2019**, *4*, 169−188.

(89) Stoumpos, C. C.; Kanatzidis, M. G. Halide Perovskites: Poor Man's High-Performance Semiconductors. *Adv. Mater.* **2016**, *28*, 5778−5793.

(90) Sopiha, K. V.; Comparotto, C.; Márquez, J. A.; Scragg, J. J. S. Chalcogenide Perovskites: Tantalizing Prospects, Challenging Materials. *Adv. Opt. Mater.* **2022**, *10*, 2101704.

(91) Kobayashi, Y.; Tsujimoto, Y.; Kageyama, H. Property Engineering in Perovskites via Modification of Anion Chemistry. *Annu. Rev. Mater. Res.* **2018**, *48*, 303−326.

(92) Schaak, R. E.; Avdeev, M.; Lee, W.-L.; Lawes, G.; Zandbergen, H. W.; Jorgensen, J. D.; Ong, N. P.; Ramirez, A. P.; Cava, R. J. Formation of Transition Metal Boride and Carbide Perovskites Related to Superconducting $MgCNi_3$. *J. Solid State Chem.* **2004**, *177*, 1244−1251.

(93) Li, W.; Wang, Z.; Deschler, F.; Gao, S.; Friend, R. H.; Cheetham, A. K. Chemically Diverse and Multifunctional Hybrid Organic−Inorganic Perovskites. *Nat. Rev. Mater.* **2017**, *2*, 1−18.

(94) Shamsi, J.; Urban, A. S.; Imran, M.; De Trizio, L.; Manna, L. Metal Halide Perovskite Nanocrystals: Synthesis, Post-Synthesis Modifications, and Their Optical Properties. *Chem. Rev.* **2019**, *119*, 3296−3348.

(95) Kwei, G. H.; Lawson, A. C.; Billinge, S. J. L.; Cheong, S. W. Structures of the Ferroelectric Phases of Barium Titanate. *J. Phys. Chem.* **1993**, *97*, 2368−2377.

(96) Cava, R. J.; Batlogg, B.; van Dover, R. B.; Murphy, D. W.; Sunshine, S.; Siegrist, T.; Remeika, J. P.; Rietman, E. A.; Zahurak, S.; Espinosa, G. P. Bulk Superconductivity at 91 K in Single-Phase Oxygen-Deficient Perovskite $Ba_2YCu_3O_{9-\delta}$. *Phys. Rev. Lett.* **1987**, *58*, 1676−1679.

(97) Akkerman, Q. A.; Manna, L. What Defines a Halide Perovskite? *ACS Energy Lett.* **2020**, *5*, 604−610.

(98) Breternitz, J.; Schorr, S. What Defines a Perovskite? *Adv. Energy Mater.* **2018**, *8*, 180266.

(99) Fop, S.; McCombie, K. S.; Wildman, E. J.; Skakle, J. M. S.; Mclaughlin, A. C. Hexagonal Perovskite Derivatives: A New Direction in the Design of Oxide Ion Conducting Materials. *Chem. Commun.* **2019**, *55*, 2127−2137.

(100) Rodríguez-Carvajal, J.; Hennion, M.; Moussa, F.; Moudden, A. H.; Pinsard, L.; Revcolevschi, A. Neutron-Diffraction Study of the Jahn-Teller Transition in Stoichiometric $LaMnO_3$. *Phys. Rev. B* **1998**, *57*, R3189−R3192.

(101) Sánchez, D.; Alonso, J. A.; García-Hernández, M.; Martínez-Lope, M. J.; Martínez, J. L.; Mellergård, A. Origin of Neutron Magnetic Scattering in Antisite-Disordered Sr_2FeMoO_6 Double Perovskites. *Phys. Rev. B* **2002**, *65*, 104426.

(102) Yang, M.; Oró-Solé, J.; Rodgers, J. A.; Jorge, A. B.; Fuertes, A.; Attfield, J. P. Anion Order in Perovskite Oxynitrides. *Nat. Chem.* **2011**, *3*, 47−52.

(103) Evans, H. A.; Wu, Y.; Seshadri, R.; Cheetham, A. K. Perovskite-Related ReO_3-Type Structures. *Nat. Rev. Mater.* **2020**, *5*, 196−213.

(104) Yao, Y.; Sang, D.; Zou, L.; Wang, Q.; Liu, C. A Review on the Properties and Applications of WO_3 Nanostructure−Based Optical and Electronic Devices. *Nanomaterials* **2021**, *11*, 2136.

(105) Novak, T. G.; Kim, J.; DeSario, P. A.; Jeon, S. Synthesis and Applications of WO_3 Nanosheets: The Importance of Phase, Stoichiometry, and Aspect Ratio. *Nanoscale Adv.* **2021**, *3*, 5166−5182.

(106) Stanley, R. K.; Morris, R. C.; Moulton, W. G. Conduction Properties of the Hexagonal Tungsten Bronze, Rb_xWO_3. *Phys. Rev. B* **1979**, *20*, 1903−1914.

(107) Wu, H.; Chen, W. Copper Nitride Nanocubes: Size-Controlled Synthesis and Application as Cathode Catalyst in Alkaline Fuel Cells. *J. Am. Chem. Soc.* **2011**, *133*, 15236−15239.

(108) Vaughn II, D. D.; Araujo, J.; Meduri, P.; Callejas, J. F.; Hickner, M. A.; Schaak, R. E. Solution Synthesis of Cu_3PdN Nanocrystals as Ternary Metal Nitride Electrocatalysts for the Oxygen Reduction Reaction. *Chem. Mater.* **2014**, *26*, 6226−6232.

(109) Lord, R. W.; Holder, C. F.; Fenton, J. L.; Schaak, R. E. Seeded Growth of Metal Nitrides on Noble-Metal Nanoparticles To Form Complex Nanoscale Heterostructures. *Chem. Mater.* **2019**, *31*, 4605−4613.

(110) Niewa, R. Metal-Rich Ternary Perovskite Nitrides. *Eur. J. Inorg. Chem.* **2019**, *2019*, 3647−3660.

(111) Iyo, A.; Fujihisa, H.; Gotoh, Y.; Ishida, S.; Ninomiya, H.; Yoshida, Y.; Eisaki, H.; Hirose, H. T.; Terashima, T.; Kawashima, K. Structural Phase Transitions and Superconductivity Induced in Antiperovskite Phosphide $CaPd_3P$. *Inorg. Chem.* **2020**, *59*, 12397−12403.

(112) Nuss, J.; Mühle, C.; Hayama, K.; Abdolazimi, V.; Takagi, H. Tilting Structures in Inverse Perovskites, M_3TtO (M = Ca, Sr, Ba, Eu; Tt = Si, Ge, Sn, Pb). *Acta Cryst. B* **2015**, *71*, 300−312.

(113) Stadelmaier, H. H. Metal-Rich Metal-Metalloid Phases. In *Developments in the Structural Chemistry of Alloy Phases: Based on a symposium sponsored by the Committee on Alloy Phases of the Institute of Metals Division, the Metallurgical Society, American Institute of Mining, Metallurgical and Petroleum Engineers, Cleveland, Ohio, October, 1967;*

Giessen, B. C., Ed.; Springer US: Boston, MA, 1969; pp 141−180. DOI: 10.1007/978-1-4899-5564-7_6.

(114) Simon, A. Group 1 and 2 Suboxides and Subnitrides — Metals with Atomic Size Holes and Tunnels. *Coord. Chem. Rev.* **1997**, *163*, 253−270.

(115) He, T.; Huang, Q.; Ramirez, A. P.; Wang, Y.; Regan, K. A.; Rogado, N.; Hayward, M. A.; Haas, M. K.; Slusky, J. S.; Inumara, K.; Zandbergen, H. W.; Ong, N. P.; Cava, R. J. Superconductivity in the Non-Oxide Perovskite $MgCNi_3$. *Nature* **2001**, *411*, 54−56.

(116) Zhao, Y.; Daemen, L. L. Superionic Conductivity in Lithium-Rich Anti-Perovskites. *J. Am. Chem. Soc.* **2012**, *134*, 15042−15047.

(117) Song, H. M.; Kim, W. S.; Lee, Y. B.; Hong, J. H.; Lee, H. G.; Hur, N. H. Chemically Ordered $FePt_3$ Nanoparticles Synthesized by a Bimetallic Precursor and Their Magnetic Transitions. *J. Mater. Chem.* **2009**, *19*, 3677−3681.

(118) Stamenkovic, V. R.; Mun, B. S.; Arenz, M.; Mayrhofer, K. J. J.; Lucas, C. A.; Wang, G.; Ross, P. N.; Markovic, N. M. Trends in Electrocatalysis on Extended and Nanoscale Pt-Bimetallic Alloy Surfaces. *Nat. Mater.* **2007**, *6*, 241−247.

(119) Gasperin, M. Dititanate de Lanthane. *Acta Cryst. B* **1975**, *31*, 2129−2130.

(120) Teneze, N.; Mercurio, D.; Trolliard, G.; Frit, B. Cation-Deficient Perovskite-Related Compounds $(Ba,La)_nTi_{n-1}O_{3n}$ (n = 4, 5, and 6): A Rietveld Refinement from Neutron Powder Diffraction Data. *Mater. Res. Bull.* **2000**, *35*, 1603−1614.

(121) Dion, M.; Ganne, M.; Tournoux, M. Nouvelles Familles de Phases $M^IM^{II}_2Nb_3O_{10}$ a Feuillets "Perovskites. *Mater. Res. Bull.* **1981**, *16*, 1429−1435.

(122) Jacobson, A. J.; Johnson, J. W.; Lewandowski, J. T. Interlayer Chemistry between Thick Transition-Metal Oxide Layers: Synthesis and Intercalation Reactions of $K[Ca_2Na_{n-3}Nb_nO_{3n+1}]$ ($3 \leq n \leq 7$). *Inorg. Chem.* **1985**, *24*, 3727−3729.

(123) Ruddlesden, S. N.; Popper, P. New Compounds of the K_2NIF_4 Type. *Acta Crystallogr.* **1957**, *10*, 538−539.

(124) Ruddlesden, S. N.; Popper, P. The Compound $Sr_3Ti_2O_7$ and Its Structure. *Acta Crystallogr.* **1958**, *11*, 54−55.

(125) Mao, L.; Ke, W.; Pedesseau, L.; Wu, Y.; Katan, C.; Even, J.; Wasielewski, M. R.; Stoumpos, C. C.; Kanatzidis, M. G. Hybrid Dion−Jacobson 2D Lead Iodide Perovskites. *J. Am. Chem. Soc.* **2018**, *140*, 3775−3783.

(126) Li, J.; Yu, Q.; He, Y.; Stoumpos, C. C.; Niu, G.; Trimarchi, G. G.; Guo, H.; Dong, G.; Wang, D.; Wang, L.; Kanatzidis, M. G. $Cs_2PbI_2Cl_2$, All-Inorganic Two-Dimensional Ruddlesden−Popper Mixed Halide Perovskite with Optoelectronic Response. *J. Am. Chem. Soc.* **2018**, *140*, 11085−11090.

(127) Hervoches, C. H.; Lightfoot, P. A Variable-Temperature Powder Neutron Diffraction Study of Ferroelectric $Bi_4Ti_3O_{12}$. *Chem. Mater.* **1999**, *11*, 3359−3364.

(128) Sun, Y.; Zhang, W.; Xing, Y.; Li, F.; Zhao, Y.; Xia, Z.; Wang, L.; Ma, X.; Xue, Q.-K.; Wang, J. High Temperature Superconducting FeSe Films on $SrTiO_3$ Substrates. *Sci. Rep.* **2014**, *4*, 6040.

(129) Shatruk, M. $ThCr_2Si_2$ Structure Type: The "Perovskite" of Intermetallics. *J. Solid State Chem.* **2019**, *272*, 198−209.

(130) Rahaman, Md. Z.; Rahman, Md. A. $ThCr_2Si_2$-Type Ru-Based Superconductors $LaRu_2M_2$ (M = P and As): An *Ab-Initio* Investigation. *J. Alloys Compd.* **2017**, *695*, 2827−2834.

(131) Ozaki, D.; Suzuki, H.; Ogawa, K.; Sakamoto, R.; Inaguma, Y.; Nakashima, K.; Tomita, O.; Kageyama, H.; Abe, R. Synthesis, Band Structure and Photocatalytic Properties of Sillén−Aurivillius Oxy-chlorides $BaBi_5Ti_3O_{14}Cl$, $Ba_2Bi_5Ti_4O_{17}Cl$ and $Ba_3Bi_5Ti_5O_{20}Cl$ with Triple-, Quadruple- and Quintuple-Perovskite Layers. *J. Mater. Chem. A* **2021**, *9*, 8332−8340.

(132) Bannister, F. A. The Crystal-Structure of the Bismuth Oxyhalides. *Mineralogical Magazine and Journal of the Mineralogical Society* **1935**, *24*, 49−58.

(133) Zachariasen, W. H. Crystal Chemical Studies of the 5f-Series of Elements. XIV. Oxyfluorides, XOF. *Acta Crystallogr.* **1951**, *4*, 231−236.

(134) Cheng, H.; Huang, B.; Dai, Y. Engineering BiOX (X = Cl, Br, I) Nanostructures for Highly Efficient Photocatalytic Applications. *Nanoscale* **2014**, *6*, 2009−2026.

(135) Kim, D.; Park, S.; Kim, S.; Kang, S.-G.; Park, J.-C. Blue-Emitting Eu^{2+}-Activated LaOX (X = Cl, Br, and I) Materials: Crystal Field Effect. *Inorg. Chem.* **2014**, *53*, 11966−11973.

(136) Wood, C. H.; Schaak, R. E. Topochemical Anionic Subunit Insertion Reaction for Constructing Nanoparticles of Layered Oxy-chalcogenide Intergrowth Structures. *J. Am. Chem. Soc.* **2023**, *145*, 18711−18715.

(137) Khan, Z.; Singh, P.; Ansari, S. A.; Manippady, S. R.; Jaiswal, A.; Saxena, M. VO$_2$ Nanostructures for Batteries and Supercapacitors: A Review. *Small* **2021**, *17*, 2006651.

(138) Zylbersztejn, A.; Mott, N. F. Metal-Insulator Transition in Vanadium Dioxide. *Phys. Rev. B* **1975**, *11*, 4383−4395.

(139) Liang, Q.; Zhang, Q.; Zhao, X.; Liu, M.; Wee, A. T. S. Defect Engineering of Two-Dimensional Transition-Metal Dichalcogenides: Applications, Challenges, and Opportunities. *ACS Nano* **2021**, *15*, 2165−2181.

(140) Lin, Z.; Carvalho, B. R.; Kahn, E.; Lv, R.; Rao, R.; Terrones, H.; Pimenta, M. A.; Terrones, M. Defect Engineering of Two-Dimensional Transition Metal Dichalcogenides. *2D Mater.* **2016**, *3*, 022002.

(141) Singh, S.; Ryan, K. M. Occurrence of Polytypism in Compound Colloidal Metal Chalcogenide Nanocrystals, Opportunities, and Challenges. *J. Phys. Chem. Lett.* **2015**, *6*, 3141−3148.

(142) Ferro, R.; Saccone, A. *Intermetallic Chemistry*; Elsevier, 2011.

(143) Zhou, M.; Li, C.; Fang, J. Noble-Metal Based Random Alloy and Intermetallic Nanocrystals: Syntheses and Applications. *Chem. Rev.* **2021**, *121*, 736−795.

(144) Sun, S.; Murray, C. B.; Weller, D.; Folks, L.; Moser, A. Monodisperse FePt Nanoparticles and Ferromagnetic FePt Nano-crystal Superlattices. *Science* **2000**, *287*, 1989−1992.

(145) Li, J.; Li, J.; Luo, J.; Wang, L.; He, X. Recent Advances in the LiFeO2-Based Materials for Li-Ion Batteries. *Int. J. Electrochem. Sci.* **2011**, *6*, 1550−1561.

(146) Shirane, T.; Kanno, R.; Kawamoto, Y.; Takeda, Y.; Takano, M.; Kamiyama, T.; Izumi, F. Structure and Physical Properties of Lithium Iron Oxide, LiFeO$_2$, Synthesized by Ionic Exchange Reaction. *Solid State Ion.* **1995**, *79*, 227−233.

(147) Zhou, Y.; Zhou, Z.; Chen, M.; Zong, Y.; Huang, J.; Pang, S.; Padture, N. P. Doping and Alloying for Improved Perovskite Solar Cells. *J. Mater. Chem. A* **2016**, *4*, 17623−17635.

(148) Löffler, T.; Savan, A.; Garzón-Manjón, A.; Meischein, M.; Scheu, C.; Ludwig, A.; Schuhmann, W. Toward a Paradigm Shift in Electrocatalysis Using Complex Solid Solution Nanoparticles. *ACS Energy Lett.* **2019**, *4*, 1206−1214.

(149) George, E. P.; Raabe, D.; Ritchie, R. O. High-Entropy Alloys. *Nat. Rev. Mater.* **2019**, *4*, 515−534.

(150) Dey, G. R.; Soliman, S. S.; McCormick, C. R.; Wood, C. H.; Katzbaer, R. R.; Schaak, R. E. Colloidal Nanoparticles of High Entropy Materials: Capabilities, Challenges, and Opportunities in Synthesis and Characterization. *ACS Nanosci. Au* **2024**, *4*, 3−20.

(151) Sun, Y.; Dai, S. High-Entropy Materials for Catalysis: A New Frontier. *Sci. Adv.* **2021**, *7*, No. eabg1600.

(152) Mantella, V.; Ninova, S.; Saris, S.; Loiudice, A.; Aschauer, U.; Buonsanti, R. Synthesis and Size-Dependent Optical Properties of Intermediate Band Gap Cu$_3$VS$_4$ Nanocrystals. *Chem. Mater.* **2019**, *31*, 532−540.

(153) Chang, C.-Y.; Prado-Rivera, R.; Liu, M.; Lai, C.-Y.; Radu, D. R. Colloidal Synthesis and Photocatalytic Properties of Cu$_3$NbS$_4$ and Cu$_3$NbSe$_4$ Sulvanite Nanocrystals. *ACS Nanosci. Au* **2022**, *2*, 440−447.

(154) Uchiumi, T.; Shirotani, I.; Sekine, C.; Todo, S.; Yagi, T.; Nakazawa, Y.; Kanoda, K. Superconductivity of LaRu$_4$X$_{12}$ (X = P, As and Sb) with Skutterudite Structure. *J. Phys. Chem. Solids* **1999**, *60*, 689−695.

(155) Weller, D. P.; Stevens, D. L.; Kunkel, G. E.; Ochs, A. M.; Holder, C. F.; Morelli, D. T.; Anderson, M. E. Thermoelectric Performance of Tetrahedrite Synthesized by a Modified Polyol Process. *Chem. Mater.* **2017**, *29*, 1656−1664.

(156) van Embden, J.; Latham, K.; Duffy, N. W.; Tachibana, Y. Near-Infrared Absorbing Cu$_{12}$Sb$_4$S$_{13}$ and Cu$_3$SbS$_4$ Nanocrystals: Synthesis, Characterization, and Photoelectrochemistry. *J. Am. Chem. Soc.* **2013**, *135*, 11562−11571.

(157) Rajamani, V.; Prewitt, C. T. Refinement of the Structure of Co$_9$S$_8$. *Can. Mineral.* **1975**, *13*, 75−78.

(158) Callejas, J. F.; Read, C. G.; Roske, C. W.; Lewis, N. S.; Schaak, R. E. Synthesis, Characterization, and Properties of Metal Phosphide Catalysts for the Hydrogen-Evolution Reaction. *Chem. Mater.* **2016**, *28*, 6017−6044.

(159) Pei, Y.; Cheng, Y.; Chen, J.; Smith, W.; Dong, P.; Ajayan, P. M.; Ye, M.; Shen, J. Recent Developments of Transition Metal Phosphides as Catalysts in the Energy Conversion Field. *J. Mater. Chem. A* **2018**, *6*, 23220−23243.

(160) Popczun, E. J.; Read, C. G.; Roske, C. W.; Lewis, N. S.; Schaak, R. E. Highly Active Electrocatalysis of the Hydrogen Evolution Reaction by Cobalt Phosphide Nanoparticles. *Angew. Chem., Int. Ed.* **2014**, *53*, 5427−5430.

(161) Li, X.; Xing, W.; Hu, T.; Luo, K.; Wang, J.; Tang, W. Recent Advances in Transition-Metal Phosphide Electrocatalysts: Synthetic Approach, Improvement Strategies and Environmental Applications. *Coord. Chem. Rev.* **2022**, *473*, 214811.

(162) Von Schnering, H.-G.; Hönle, W. Bridging Chasms with Polyphosphides. *Chem. Rev.* **1988**, *88*, 243−273.

(163) Freymeyer, N. J.; Cunningham, P. D.; Jones, E. C.; Golden, B. J.; Wiltrout, A. M.; Plass, K. E. Influence of Solvent Reducing Ability on Copper Sulfide Crystal Phase. *Cryst. Growth Des.* **2013**, *13*, 4059−4065.

(164) Knowles, K. E.; Hartstein, K. H.; Kilburn, T. B.; Marchioro, A.; Nelson, H. D.; Whitham, P. J.; Gamelin, D. R. Luminescent Colloidal Semiconductor Nanocrystals Containing Copper: Synthesis, Photo-physics, and Applications. *Chem. Rev.* **2016**, *116*, 10820−10851.

(165) Schaak, R. E.; Steimle, B. C.; Fenton, J. L. Made-to-Order Heterostructured Nanoparticle Libraries. *Acc. Chem. Res.* **2020**, *53*, 2558−2568.

(166) Li, Z.; Saruyama, M.; Asaka, T.; Tatetsu, Y.; Teranishi, T. Determinants of Crystal Structure Transformation of Ionic Nanocryst-als in Cation Exchange Reactions. *Science* **2021**, *373*, 332−337.

(167) Roy, P.; Srivastava, S. K. Nanostructured Copper Sulfides: Synthesis, Properties and Applications. *CrystEngComm* **2015**, *17*, 7801−7815.

(168) Steimle, B. C.; Lord, R. W.; Schaak, R. E. Phosphine-Induced Phase Transition in Copper Sulfide Nanoparticles Prior to Initiation of a Cation Exchange Reaction. *J. Am. Chem. Soc.* **2020**, *142*, 13345−13349.

(169) Zhuang, J.; Wu, H.; Yang, Y.; Cao, Y. C. Supercrystalline Colloidal Particles from Artificial Atoms. *J. Am. Chem. Soc.* **2007**, *129*, 14166−14167.

(170) Chen, J.; Ye, X.; Oh, S. J.; Kikkawa, J. M.; Kagan, C. R.; Murray, C. B. Bistable Magnetoresistance Switching in Exchange-Coupled CoFe$_2$O$_4$−Fe$_3$O$_4$ Binary Nanocrystal Superlattices by Self-Assembly and Thermal Annealing. *ACS Nano* **2013**, *7*, 1478−1486.

(171) Ye, X.; Chen, J.; Diroll, B. T.; Murray, C. B. Tunable Plasmonic Coupling in Self-Assembled Binary Nanocrystal Superlattices Studied by Correlated Optical Microspectrophotometry and Electron Micros-copy. *Nano Lett.* **2013**, *13*, 1291−1297.

(172) Shevchenko, E. V.; Talapin, D. V.; Murray, C. B.; O'Brien, S. Structural Characterization of Self-Assembled Multifunctional Binary Nanoparticle Superlattices. *J. Am. Chem. Soc.* **2006**, *128*, 3620−3637.

(173) Wang, Y.; Chen, J.; Zhong, Y.; Jeong, S.; Li, R.; Ye, X. Structural Diversity in Dimension-Controlled Assemblies of Tetrahedral Gold Nanocrystals. *J. Am. Chem. Soc.* **2022**, *144*, 13538−13546.